Cellular/Molecular

The Structural and Functional Integrity of Rod Photoreceptor Ribbon Synapses Depends on Redundant Actions of Dynamins 1 and 3

Christin Hanke-Gogokhia,[1] Thomas E. Zapadka,[1,2] Stella Finkelstein,[3] Mikael Klingeborn,[3*] Timothy K. Maugel,[4] Joshua H. Singer,[4] Vadim Y. Arshavsky,[3] and Jonathan B. Demb[1,2,5,6]

Departments of [1]Ophthalmology & Visual Science, [2]Cellular & Molecular Physiology, Yale University, New Haven, Connecticut 06511, [3]Department of Ophthalmology, Duke University School of Medicine, Durham, North Carolina 27705, [4]Department of Biology, University of Maryland, College Park, Maryland 20742, [5]Department of Neuroscience, Yale University, New Haven, Connecticut 06511, and [6]Wu Tsai Institute, Yale University, New Haven, Connecticut 06511

Vertebrate vision begins with light absorption by rod and cone photoreceptors, which transmit signals from their synaptic terminals to second-order neurons: bipolar and horizontal cells. In mouse rods, there is a single presynaptic ribbon-type active zone at which the release of glutamate occurs tonically in the dark. This tonic glutamatergic signaling requires continuous exo- and endocytosis of synaptic vesicles. At conventional synapses, endocytosis commonly requires dynamins: GTPases encoded by three genes (*Dnm1–3*), which perform membrane scission. Disrupting endocytosis by dynamin deletions impairs transmission at conventional synapses, but the impact of disrupting endocytosis and the role(s) of specific dynamin isoforms at rod ribbon synapses are understood incompletely. Here, we used cell-specific knock-outs (KOs) of the neuron-specific *Dnm1* and *Dnm3* to investigate the functional roles of dynamin isoforms in rod photoreceptors in mice of either sex. Analysis of synaptic protein expression, synapse ultrastructure, and retinal function via electroretinograms (ERGs) showed that dynamins 1 and 3 act redundantly and are essential for supporting the structural and functional integrity of rod ribbon synapses. Single *Dnm3* KO showed no phenotype, and single *Dnm1* KO only modestly reduced synaptic vesicle density without affecting vesicle size and overall synapse integrity, whereas double *Dnm1/Dnm3* KO impaired vesicle endocytosis profoundly, causing enlarged vesicles, reduced vesicle density, reduced ERG responses, synaptic terminal degeneration, and disassembly and degeneration of postsynaptic processes. Concurrently, cone function remained intact. These results show the fundamental redundancy of dynamins 1 and 3 in regulating the structure and function of rod ribbon synapses.

Key words: **dynamin; endocytosis; retina; ribbon; rod photoreceptor; synapse**

Significance Statement

The process of vision starts with the capturing of light by rod and cone photoreceptors within the retina. Photoreceptors communicate with downstream retinal neurons at specialized sites called ribbon synapses, where vesicles filled with the neurotransmitter glutamate are released and recycled. The synaptic vesicle recycling process at conventional synapses commonly requires specialized proteins for membrane scission, typically dynamins 1 and 3. The role of dynamins in vesicle cycling at photoreceptor ribbon synapses, however, is not fully understood. Here, we specifically deleted dynamins 1 and 3 in rod photoreceptors using a conditional gene knock-out approach and demonstrated the redundant role of dynamins 1 and 3 in maintaining rod photoreceptor ribbon synapse structure and function.

Received July 21, 2023; revised April 2, 2024; accepted April 13, 2024.

Author contributions: C.H.-G., J.H.S., V.Y.A., and J.B.D. designed research; C.H.-G., T.E.Z., S.F., M.K., T.K.M., and J.H.S. performed research; C.H.-G., T.E.Z., and J.H.S. analyzed data; C.H.-G., V.Y.A., and J.B.D. wrote the paper.

This work was supported by NIH Grants F32 EY032389, F31 EY034776, T32 EY022312, R01 EY014454, R01 EY017836, R01 EY030451, P30 EY026878, and P30 EY005722, an unrestricted grant from Research to Prevent Blindness (Duke University), and research funds from the University of Maryland.

The authors declare no competing financial interests.

[*]M.K.'s present address: McLaughlin Research Institute, Great Falls, Montana 59405

Correspondence should be addressed to Jonathan B. Demb at jonathan.demb@yale.edu or Vadim Y. Arshavsky at vadim.arshavsky@duke.edu.

https://doi.org/10.1523/JNEUROSCI.1379-23.2024

Introduction

Vertebrate photoreceptors, rods and cones, absorb light in their outer segments to generate the electrical signal that underlies the first step in vision (Arshavsky and Burns, 2012). Rods are more sensitive and mediate vision in dim light, whereas cones mediate vision in bright light. Light-dependent changes in membrane potential modulate glutamate release from photoreceptor synaptic terminals onto second-order bipolar and horizontal cells (HCs) (Fig. 1; Furukawa et al., 2020; Burger et al., 2021).

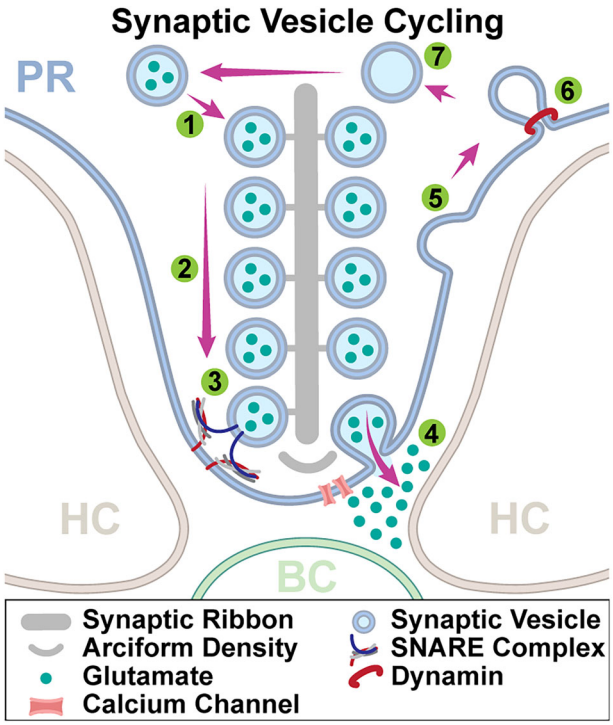

Figure 1. Working model for synaptic vesicle cycling at the rod ribbon synapse. Cytoplasmic vesicles attach and replenish vacant sites on the ribbon (1). As tethered vesicles move down the ribbon (2), they are primed for release (3). At the base, the opening of L-type calcium channels allows an influx of Ca^{2+} and triggers the fusion of vesicles with the plasma membrane. Vesicle exocytosis releases glutamate into the synaptic cleft (4). Vesicular proteins and lipids released into the membrane are removed via vesicle endocytosis. Membrane invagination occurs (5) followed by scission of the formed vesicle from the plasma membrane by dynamin (6). Reformed vesicles are refilled with glutamate (7) and returned to the large cytoplasmic pool of vesicles.

Photoreceptor presynaptic active zones are so-called ribbon synapses owing to the platelike, electron-dense, proteinaceous structures composed largely of the protein RIBEYE (Schmitz et al., 2000) that tether glutamate-filled vesicles near presynaptic Ca channels (Sterling and Matthews, 2005; Thoreson, 2021). Despite their unique structure, photoreceptor synapses contain much of the presynaptic cellular machinery that operates at conventional synapses (Fig. 1; Schmitz et al., 2000; Dick et al., 2003; tom Dieck et al., 2005; Johnson et al., 2007; Muller et al., 2019). Ca^{2+}-dependent exocytosis begins with the opening of Cav1.4-containing Ca channels mediating L-type currents (Haeseleer et al., 2004; Mercer et al., 2011; Pangrsic et al., 2018; Waldner et al., 2018; Maddox et al., 2020) and is mediated by conventional SNARE proteins (Burger et al., 2021) and complexin 3 (Reim et al., 2009) with synaptotagmin-1 (Syt1) acting as the primary Ca^{2+} sensor; Syt7 plays a secondary role (Grassmeyer et al., 2019; Mesnard et al., 2022).

Photoreceptor release rates are high in the dark when photoreceptors are depolarized. For example, rods release ~10–20 vesicles/sec/synapse (Sheng et al., 2007; Hays et al., 2020). Light hyperpolarizes the rod and suppresses vesicular release (Field and Rieke, 2002; Hays et al., 2021). The high rate of exocytosis in rods requires a similarly high rate of endocytosis (vesicle retrieval) to sustain synaptic transmission (LoGiudice and Matthews, 2007; Mercer and Thoreson, 2011). At a conventional synapse, endocytosis includes the critical step of membrane scission—severing of a vesicle budding from the plasma membrane—commonly performed by dynamin GTPases (Fig. 1; Ferguson et al., 2007, 2009; Raimondi et al., 2011; Ferguson and De Camilli, 2012; Wu et al., 2014; Antonny et al., 2016; Fan et al., 2016). Three dynamin isoforms, encoded by individual genes (*Dnm1–3*; Praefcke and McMahon, 2004), have distinct expression patterns and functions (Ramachandran, 2011). Dynamin 1 is expressed exclusively and dominantly in the brain; dynamin 3 is also expressed in the brain as well as the testis; and dynamin 2 plays a ubiquitous housekeeping role in cell function and its deletion is embryonically lethal (Ferguson et al., 2007, 2009; Ferguson and De Camilli, 2012).

Global deletion of dynamin 1 causes death within the first 2 postnatal weeks, whereas deletion of dynamin 3 lacks a phenotype (Ferguson et al., 2007; Raimondi et al., 2011). Nevertheless, deletion of dynamin 3 can worsen the dynamin 1 knock-out (KO) phenotype in some experimental systems, suggesting overlapping functions between the two isoforms (Raimondi et al., 2011; Fan et al., 2016). Indeed, the combined KO of both neuronal dynamins, *Dnm1* and *Dnm3*, results in depletion of synaptic vesicles and formation of clathrin-coated pits budding from long invaginations of the plasma membrane when assessed in cultured cortical neurons (Ferguson and De Camilli, 2012).

The mechanism for endocytosis and the function of dynamins at mammalian rod synapses are incompletely understood. Mouse rods apparently express all three dynamin isoforms (Sherry and Heidelberger, 2005; Xi et al., 2007; Grossman et al., 2013; Wahl et al., 2013; Fuchs et al., 2014), and, in salamander rods, short-term inhibition of dynamin impairs synaptic vesicle endocytosis and synaptic transmission (Van Hook and Thoreson, 2012; Wen et al., 2018). Here, using conditional KO of *Dnm1* and *Dnm3* from mouse rods, we reveal the roles of these isoforms at rod ribbon synapses and elucidate the impact of dynamin deletions on photoreceptor synapses and the integrity of postsynaptic neurons.

Materials and Methods

Generation of conditional dynamins 1 and 3 KO mice. Mice containing floxed alleles of dynamin 1 ($Dnm1^{fl/fl}$) and dynamin 3 ($Dnm3^{fl/fl}$) were kindly provided by Pietro De Camilli (Yale University). For $Dnm1^{fl/fl}$ mice, loxP sites flank exons 2–4 of *Dnm1* (Ferguson et al., 2009); and for $Dnm3^{fl/fl}$ mice, loxP sites flank exon 2 of *Dnm3* (Raimondi et al., 2011). These mice were crossed to transgenic *iCre75* (*Rhodopsin-iCre*) mice (Li et al., 2005) to obtain conditional deletion of *Dnm1* and *Dnm3* in rod photoreceptors ($^{rod}Dnm1^{-/-}$ and $^{rod}Dnm3^{-/-}$); $Dnm1^{fl/fl}$ or $Dnm3^{fl/fl}$ littermate mice were used as controls throughout this study. We confirmed the deletion of *Dnm1* and *Dnm3* in rods by in-house PCR. Genomic DNA was isolated from mouse tails using the Qiagen kit (#69506), and genotyping PCR was performed using the following 5′ end-primer set:

Dyn1cKO-AS2: TTGTGTATGTGAGTGCACCCATGC;
Dyn1cKO-S2: CAGCTGGGTATAATGAGGCCTCATC;
Dyn3cKO_LoxpS1: CAGTGCCTTCCAAGTTCAATTCC;
Dyn3cKO_LoxpAS1: GACATGTTAACATAGGCTAAACC;
iCre75-F: GGATGCCACCTCTGATGAAG;
iCre75-R: CACACCATTCTTTCTGACCCG.

PCR for *Dnm1* yields an amplicon of 230 bp for the wild-type allele and 300 bp for the mutant allele. PCR for *Dnm3* yields an amplicon of 200 bp for the wild-type allele and 300 bp for the mutant allele. We also obtained germline *Dnm3* KO mice (kindly provided by Ege T. Kavalali, Vanderbilt University) for ultrastructural analysis of rod synaptic terminals. *Dnm1/Dnm3* double conditional knock-out (cKO) mice were crossed to *GNAT2* KO mice (kindly provided by A.P. Sampath, UCLA; Ronning et al., 2018) to isolate rod-specific function

for electroretinography (ERG) experiments. In some cases, genotyping was performed by Transnetyx using real-time PCR. We confirmed the absence of *rd1* and *rd8* mutations in end-use animals, as previously described (Qiao et al., 2003; Mattapallil et al., 2012); the *rd8* mutation was bred out of the original floxed mice. Mouse colony maintenance and experiments were performed in accordance with procedures approved by the Institutional Animal Care and Use Committees of either Duke University or Yale University. Mice were kept under a 12/12 h light/dark cycle. Animals of either sex aged 1–6 months were included in the study.

Retinal cross section and immunofluorescence. Retinal cross sectioning was performed as previously described (Lobanova et al., 2010; Spencer et al., 2019). Briefly, mice were killed, and eyecups were placed in 4% paraformaldehyde in PBS for 1–2 h at room temperature. After fixation, eyecups were rinsed twice in PBS and embedded in 2.5% low-melting point agarose (Precisionary Instruments, SKU VF-AGT-VM). The agarose-embedded eyecups were vibratome-sectioned into 100-µm-thick slices (VT1200; Leica), which were blocked in PBS containing 5% donkey serum and 0.5% Triton X-100 for 1 h at room temperature. In most cases, sections were incubated with primary antibodies overnight at 4°C, washed three times with PBS for 10 min, and incubated for 2 h at room temperature with appropriate secondary antibodies. For anti-calbindin-1 staining, sections were incubated for 5 d with the primary antibody and 1–2 d with the secondary antibody. Stained slices were washed three times in PBS for 10 min, mounted onto slides in Fluoromount-G (Electron Microscopy Sciences), and coverslipped.

Retinal flat mounts. To prepare retinal flat mounts, we isolated the retina from the eyecup, carefully removed the vitreous, and fixed the tissue in 4% paraformaldehyde in PBS for 1 h at room temperature. Retinal flat mounts were processed for immunostaining with a protocol similar to that used for retinal cross sections (see above) and described elsewhere (Vuong et al., 2015). In brief, retinas were incubated in a blocking solution overnight at 4°C, in a primary antibody solution for 5 d at 4°C, and in a secondary solution for 2 d at 4°C. Retinas were washed three times in PBS for 20 min each at room temperature after primary and secondary antibodies were applied. For imaging, the retinas were mounted on slides in Fluoromount-G (Electron Microscopy Sciences) with the retinal ganglion cell layer facing the coverslip. For both retinal sections and flat mounts, images were taken with a Zeiss LSM800 confocal microscope. Image analysis and processing was performed with ImageJ software (ImageJ2 Version 2.3.0/1.53q).

Antibodies. The following primary antibodies were used: mouse anti-bassoon (1:500, Enzo Life Technologies, SAP7F407), mouse anti-calbindin-1 (1:500, Sigma-Aldrich, C9849), rabbit anti-calbindin-1 (1:500, Sigma-Aldrich, C2724), rabbit anti-complexin 3 (1:500, Synaptic Systems, 122-302), rabbit anti-cone arrestin (1:500, Sigma-Aldrich, AB15282), mouse anti-C-terminal-binding protein 2 (CtBP2; 1:1,000, BD Biosciences, 612044), rabbit anti-dynamin 1 (1:250, Proteintech, 182505-1-AP), rabbit anti-dynamin 3 (1:250, Synaptic Systems, 115302), rat anti-glial fibrillary acidic protein (GFAP; 1:200, Millipore, 34580/2.2B10), sheep anti-mGluR6 (1:250, gift from Dr. Kirill Martemyanov, UF Scripps Biomedical Research), mouse anti-neurofilament NF-H (1:500, BioLegend, 801701), mouse anti-PKCα (1:1,000, Abcam, AB11721), rabbit anti-PKCα (1:1,000, Abcam, AB32376), mouse anti-PMCA-ATPase (1:250, Thermo Fisher Scientific, MA3-914), mouse anti-rhodopsin 1D4 (1:1,000, Abcam, AB5417), mouse anti-Syt1 (1:500, Synaptic Systems, 105011C3), mouse anti-synaptotagmin-2 (Syt2/ZNP-1; 1:200, Zebrafish International Resource Center, University of Oregon, AB_10013783), and guinea pig anti-VGluT1 (1:1,000, Millipore, AB5905). Bound primary antibodies were visualized with appropriate secondary antibodies conjugated with Alexa Fluor 488, Alexa Fluor 647, Cy3, or Cy5 (1:500, Invitrogen, Life Technologies, or Jackson ImmunoResearch Laboratories). Conjugated Alexa Fluor 594 wheat germ agglutinin (WGA; 1:1,000, Thermo Fisher Scientific, W11262) was used to label the interphotoreceptor matrix below rod terminals and visualize neurites postsynaptic to rods (Ishikawa et al., 2015), and conjugated Alexa Fluor 488 peanut agglutinin (PNA; 1:500, Thermo Fisher, L21409) was used to visualize cones (Blanks and Johnson, 1984). Nuclei were stained with Hoechst (1:1,000, Thermo Fisher Scientific, H3569).

Synaptic ribbon contour length quantification. Synaptic ribbon contour length was quantified using confocal microscopy images, as previously described (Grabner et al., 2015). Synaptic ribbons were stained for their structural protein RIBEYE/CtBP2 (Schmitz et al., 2000; Schmitz, 2009). The ribbon contour length was measured by drawing a line through the region of the highest signal intensity along the length of the ribbon using the freehand line tool in ImageJ software (ImageJ2 Version 2.3.0/1.53q).

Transmission electron microscopy (TEM). TEM of the rod outer segments was performed at Duke University. Mice were deeply anesthetized and transcardially perfused with 2% paraformaldehyde, 2% glutaraldehyde, and 0.05% calcium chloride in 50 mM MOPS, pH 7.4, as described in Ding et al. (2015). Eyes were enucleated and fixed for an additional 2 h in the same buffer at room temperature. Fixed eyes were washed twice in PBS, and eyecups were dissected for further tissue processing using the following contrasting technique: eyecups were embedded in PBS containing 2.5% low-melting point agarose (Precisionary Instruments) and cut into 200-µm-thick slices on a vibratome (Leica VT1200). Next, the slices were stained with 1% tannic acid (Electron Microscopy Sciences) and 1% uranyl acetate (Electron Microscopy Sciences), gradually dehydrated with ethanol, and infiltrated and embedded in Spurr's resin (Electron Microscopy Sciences; Ding et al., 2015). Next, 70-nm-thin sections of the central retina were cut from resin-embedded samples, placed on copper grids, counterstained with 2% uranyl acetate and 3.5% lead citrate (Ted Pella), and imaged on a JEM-1400 electron microscope (JEOL) with a digital camera (BioSprint; AMT).

TEM of the rod synaptic terminals was performed at the University of Maryland as previously described (Park et al., 2020). Briefly, an excised retina was fixed for 1 h at room temperature with 4% paraformaldehyde, 2% glutaraldehyde, and 4 mM $CaCl_2$, pH 7.4, in 0.2 M cacodylate buffer. After fixation, the tissue was washed in four changes of 0.2 M cacodylate buffer for 20 min each on ice, followed by immersion of the tissue in 0.2 M cacodylate buffer containing 20 mM glycine for 30 min on ice. Next, the tissue was washed in five changes of 0.1 M cacodylate buffer for 10 min each on ice and stored until further processing in 0.15 M cacodylate buffer at 4°C. Ferrocyanide-reduced osmium tetroxide was used as a postfix followed by an en bloc treatment in 2% uranyl acetate before ethanol dehydration (35–100%). Next, infiltration in a propylene oxide:epoxy resin series was followed by embedding and polymerization in epoxy resin (Spurr's low-viscosity formulation, #14300, Electron Microscopy Sciences). Thin sections were cut on a Reichert-Jung UltraCut E ultramicrotome, stained with 0.2% lead citrate before being viewed and photographed on a Hitachi HT7700 transmission electron microscope.

ERG. Animals were dark adapted overnight, and anesthesia was subsequently delivered in the amount of ∼100 mg/kg ketamine and ∼10 mg/kg xylazine solution per hour. Anesthetized animals were placed on a stage with a heater to maintain appropriate body temperature. The pupils were then dilated with one drop per eye of 1% tropicamide solution and one drop of Gonak (Akorn) was applied along with careful placement of the gold wire corneal electrodes (LKC Technologies, SKU: N30). For scotopic (i.e., dim-light level) ERGs, single-flash responses were recorded at intensities of −4.0 to +2.7 log cd·s/m^2. For photopic (i.e., bright-light level) ERGs, the mice were light adapted under a background light of +1.48 log cd·s/m^2 for 5–10 min. Single-flash photopic responses were recorded at intensities of −1.0 to +2.7 log cd·s/m^2, presented on the +1.48 log cd·s/m^2 background. In these experiments, ERGs were recorded from both eyes simultaneously (Ganzfeld BigShot, LKC Technologies). ERG traces were analyzed as previously described (Herrmann et al., 2011) using programs written in MATLAB (version R2021a, MathWorks). In brief, the ERG a-wave amplitude was calculated as the negative deflection observed within the first 60 ms after the flash.

The b-wave was calculated as the maximal amplitude of positive deflection following the a-wave after applying a 55 Hz Bessel filter to remove oscillatory potentials. Scotopic ERG b-wave amplitudes were fit using Equation 1, where $R_{max,1}$ and $R_{max,2}$ are the maximal response amplitudes and $I_{0.5,1}$ and $I_{0.5,2}$ are the half-saturating flash intensities; the first term reflects pure rod responses, whereas the second term reflects mixed rod/cone responses. For the scotopic a-wave, we fit the data with a single term from Equation 1. Data were calculated individually, and results are shown as mean ± SD:

$$R = R_{\max,1}\frac{I}{I + I_{0.5,1}} + R_{\max,2}\frac{I}{I + I_{0.5,2}} \quad (1)$$

Intravitreal adeno-associated virus (AAV) injections for sparse retinal cell labeling. Intravitreal injections in adult mice were performed under continuous 1–2% isoflurane anesthesia. Using a 30 G needle, a small scleral puncture was made at ∼2 mm from the limbus, under an operating microscope. Next, 1.0 µl of AAV (3.3×10^{11} vg ml^{-1}) particles expressing GFP-channelrhodopsin-2 fusion protein under the control of the CAG promoter (AAV2/1-CAG-ChR2-GFP; UNC Vector Core) was delivered using an injection microsyringe with a blunt 33 G needle. Afterward, a topical antibiotic ointment was applied to the cornea. Thermal support was provided for the duration of the procedure and during recovery. Animals were killed 3 weeks postinjection to achieve maximal protein expression, and the retinal tissue was collected for microscopic examination. AAV-mediated GFP expression was imaged without further amplification by a primary antibody.

Statistical analyses. For statistical analysis of ERG data (Figs. 3, 4), we focused on intensity ranges that approximate the maximal rod-only response (−2 to −1 log cd·s/m^2) and mixed rod/cone response (+2 to +2.7 log cd·s/m^2) based on the apparent saturation of each response level according to the fit with Equation 1. Scotopic a-waves and photopic b-waves were analyzed only at the higher intensity range (+2 to +2.7 log cd·s/m^2), where the signal-to-noise ratio was sufficient. In Figure 3, where three genotypes were compared to control, we reduced the α in unpaired *t* tests by ten-fold to account for multiple comparisons (from 0.05 to 0.005). In Figure 4, where one genotype was compared to control, we reduced the α by five-old (from 0.05 to 0.01). All statistical analyses were carried out in Prism 9 (GraphPad).

For the analysis of the outer nuclear layer (ONL) thickness (Fig. 5), each genotype versus control typically included at least three measurements quantified from three different animals per genotype ($N = 9$ measurements per genotype). In each age group, significance was defined by one-way ANOVA and the Dunnett multiple comparisons test with α = 0.05. Significance is reported according to the multiplicity adjusted *p*-value.

For the analysis of the synaptic ribbon contour length (Fig. 6), each genotype versus control included five ribbons quantified from three regions per animal ($N = 15$ ribbons per genotype). Significance was defined by one-way ANOVA and the Dunnett multiple comparisons test with $\alpha = 0.05$ (one-tailed). Significance is reported according to the multiplicity adjusted *p*-value.

For the analysis of the synaptic vesicles (Figs. 9,10), we quantified the densities of ribbon-associated and cytoplasmic vesicles and measured the diameters of each. Ribbon-associated vesicles were taken as being within a region of quantification extending 100 nm on either side of the synaptic ribbon (Fig. 9*A*). To avoid artifacts of the tissue architecture, we did not quantify any region where the plasma membrane was closer than 100 nm to the ribbon (i.e., regions where vesicles could not exist). We then calculated the ribbon-associated vesicle density as the number of vesicles whose centroids fall within the quantification regions on both sides of the ribbon divided by the length of the quantified ribbon region.

For cytoplasmic vesicles, we identified regions of quantification that were nonadjacent to the synaptic ribbon (Fig. 9*A*). Vesicles were counted in 0.3 × 0.3 µm regions, and the cytoplasmic vesicle density is reported as the number of vesicles whose centroids fall within the quantification region divided by the quantification area. For all measurements of vesicle density, a minimum of 10 regions/ribbons from two animals per genotype were quantified. To compare vesicle density between four genotypes (Fig. 9), significance was defined by one-way ANOVA and the Dunnett multiple comparisons test with $\alpha = 0.05$. Significance is reported according to the multiplicity adjusted *p*-value. To compare two genotypes (Fig. 10), significance was defined by unpaired *t* test with α = 0.05 in two tails. *N* was defined as the number of regions or ribbons from which vesicle densities were measured.

For the measurement of vesicle diameter, each vesicle, from either ribbon-associated or cytoplasmic pools, was outlined with an ellipse. The diameter of the vesicle was estimated as the diameter of a circle with a circumference equal to that of the bounding ellipse. We included a minimum of 200 vesicles for each genotype. For statistical analyses of vesicle density, significance was defined by unpaired *t* test with $\alpha = 0.05$ in two tails. *N* was defined as the number of ribbons or regions quantified. Statistical analyses for vesicle diameters were performed in MATLAB (MathWorks R2020a).

Results

Generation of rod-specific dynamin KO mice

We crossed floxed *Dnm1* and *Dnm3* mice (*Dnm1*$^{fl/fl}$ and *Dnm3*$^{fl/fl}$; Ferguson et al., 2009; Raimondi et al., 2011) with transgenic *iCre75* mice expressing Cre recombinase under the control of the rhodopsin promoter (Li et al., 2005) to knock out dynamin specifically in rods. *Cre-loxP* recombination in rods of these mice begins at postnatal Day 7 (P7), and conditional rod-specific single (^{rod}*Dnm1*$^{-/-}$ and ^{rod}*Dnm3*$^{-/-}$) and double (^{rod}*Dnm1*$^{-/-}$/*3*$^{-/-}$) dynamin KOs were evaluated between postnatal day 28 (P28) and P180 using a combination of morphometric and functional assays.

We validated the conditional deletion of each dynamin isoform by immunostaining retinal cross sections (Fig. 2). Photoreceptor synaptic terminals were labeled with an antibody against the plasma membrane calcium ATPase (PMCA; Krizaj and Copenhagen, 1998; Krizaj et al., 2002). Cone terminals were distinguished from rod terminals by their proximity to the inner nuclear layer and their relatively larger size. Staining with anti-dynamin 1 (Fig. 2*A–D*) and anti-dynamin 3 (Fig. 2*E–H*) antibodies showed expression of both isoforms in rod and cone terminals. The staining of rod terminals was substantially reduced in both single and double cKOs analyzed at P28 (Fig. 2*B,D* for *Dnm1*; Fig. 2*G,H* for *Dnm3*), whereas dynamin staining in neighboring cone synaptic terminals remained intact (indicated with asterisk). The staining intensity of dynamin 1 in ^{rod}*Dnm3*$^{-/-}$ rods (Fig. 2*C*) was comparable to that in control mice (Fig. 2*A*) as was the staining intensity of dynamin 3 in ^{rod}*Dnm1*$^{-/-}$ rods (Fig. 2*E,F*). These results showed that dynamins 1 and 3 are present in photoreceptor synaptic terminals and validated the conditional deletion of each isoform in the corresponding cKO lines. Furthermore, the absence of dynamin immunostaining in the corresponding cKO lines validated the specificity of each antibody.

Synaptic transmission from rod synapses depends on dynamins 1 and 3

We tested the function of rods lacking dynamin isoforms using ERG. Scotopic ERGs were performed with single and double cKO mice at P28, P90, and P180 using their littermates as controls (Fig. 3*A*). We quantified two components of the ERG: the scotopic a-wave (Fig. 3*B*) and the scotopic b-wave (Fig. 3*C*). The a-wave reflects the suppression of the circulating current in photoreceptor outer segments, and the b-wave reflects the excitatory postsynaptic current in ON-bipolar cells (Robson and Frishman, 1998).

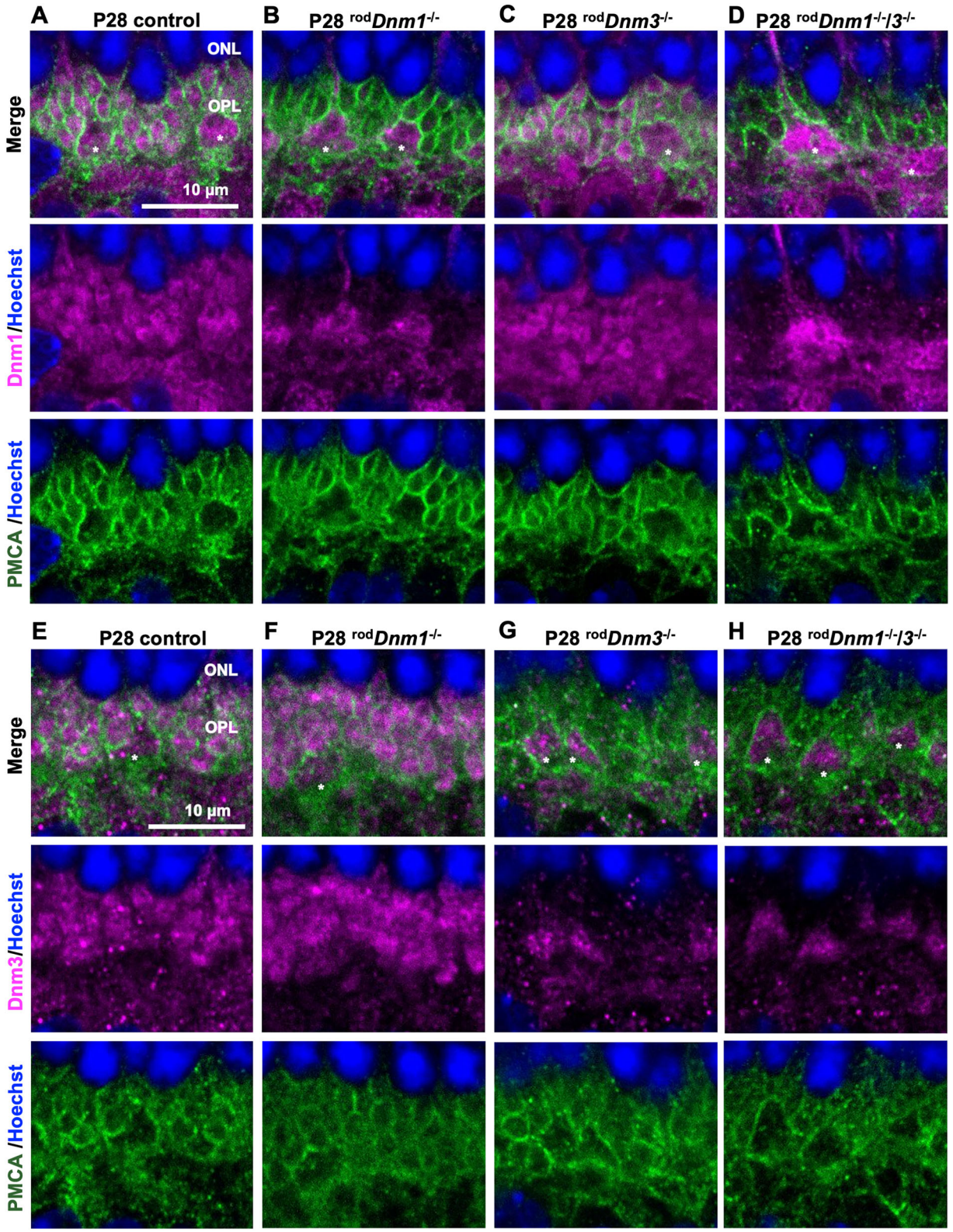

Figure 2. Conditional deletion of dynamins 1 and 3 in rod photoreceptors. Retinal cross sections were obtained at P28 and stained with antibodies against dynamin 1 (magenta; ***A–D***) and dynamin 3 (magenta; ***E–H***). Rod and cone synapses were labeled with an antibody against PMCA (green). In control mice, dynamin 1 (***A***) and dynamin 3 (***E***) are highly abundant in synaptic terminals of rod photoreceptors. Staining for dynamin 1 was absent in $^{rod}Dnm1^{-/-}$ (***B***) and $^{rod}Dnm1^{-/-}/3^{-/-}$ (***D***) mice but present in $^{rod}Dnm3^{-/-}$ mice (***C***). Staining for dynamin 3 was absent in $^{rod}Dnm3^{-/-}$ (***G***) and $^{rod}Dnm1^{-/-}/3^{-/-}$ (***H***) mice but present in $^{rod}Dnm1^{-/-}$ mice (***F***). Cone synapses, indicated with an asterisk, have normal levels of dynamin 1 and dynamin 3 staining.

The a- and b-wave amplitudes in single cKOs were indistinguishable from those of littermate controls, whereas ERGs of double cKO mice were altered significantly: the a-wave was significantly reduced at P90 and P180 (Fig. 3*B*), whereas the b-wave was significantly reduced at all three time points (Fig. 3*C*). The early reduction of the b-wave amplitude in double

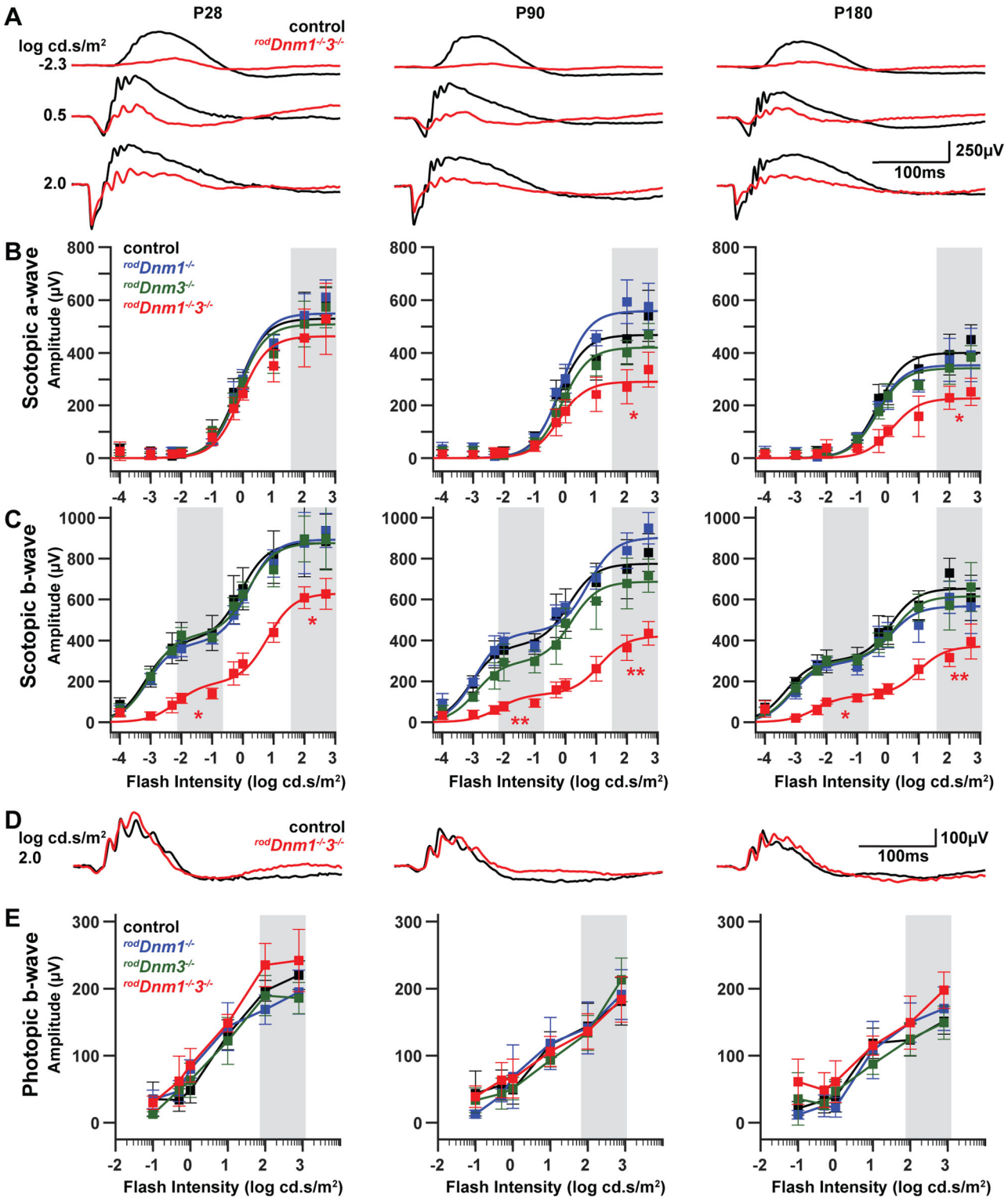

Figure 3. Scotopic ERG responses are reduced in *Dnm* double cKO mice. Average scotopic ERG responses ($n = 3–7$ animals per genotype) from control (black) and $^{rod}Dnm1^{-/-}/3^{-/-}$ (red) mice were recorded at P28, P90, and P180 at different single-flash intensities (***A***). The a-wave (***B***) and b-wave amplitudes (***C***) are plotted as a function of increasing flash intensity (mean ± SD). Scotopic ERG responses from single cKO mice ($^{rod}Dnm1^{-/-}$, blue; $^{rod}Dnm3^{-/-}$, green) were comparable to their littermate controls (black). In $^{rod}Dnm1^{-/-}/3^{-/-}$ mice (red), a significant decrease in the scotopic b-wave at P28 (***C***) is followed by a reduction in the scotopic a-wave at P90 and P180 (***B***), indicating impaired synaptic transmission to rod bipolar cells, followed by impaired photoreceptor function. ***D***, Average photopic ERG responses ($n = 3–9$ animals per genotype) from control (black) and dynamin double cKO mice (red) are shown at P28, P90, and P180 at 2.0 log cd·s/m^2. Amplitudes of photopic b-waves (***E***) were plotted over increasing intensity of single-flash stimuli. Cone-driven ERG b-waves recorded from single and double cKO mice are normal at all tested ages. Comparisons reflect average response over two flash intensities within the gray bars; $*p < 0.005$; $**p < 0.001$.

cKO mice indicates impaired synaptic transmission in rods lacking both dynamin isoforms at a time when phototransduction, as reflected by the a-wave, remained intact. The subsequent decrease in scotopic a-wave amplitude suggests either a possible defect in phototransduction or a partial loss of rods.

As a control, we assessed cone photoreceptor function in rod-specific cKO mice by measuring ERG responses in photopic conditions under which rod output is saturated (Fig. 3*D*,*E*). We found no changes in the photopic ERG responses driven by cones in double cKO animals at P28, P90, and P180 (Fig. 3*D*): photopic b-waves were normal in both single and double cKO mice at all ages (Fig. 3*E*). Thus, cone phototransduction and synaptic transmission from cones to bipolar cells remains intact in the presence of the severe rod dysfunction caused by combined *Dnm1/Dnm3* cKO.

The ERG recordings suggest that rods lacking dynamin 1/3 exhibit weak but measurable synaptic transmission with rod

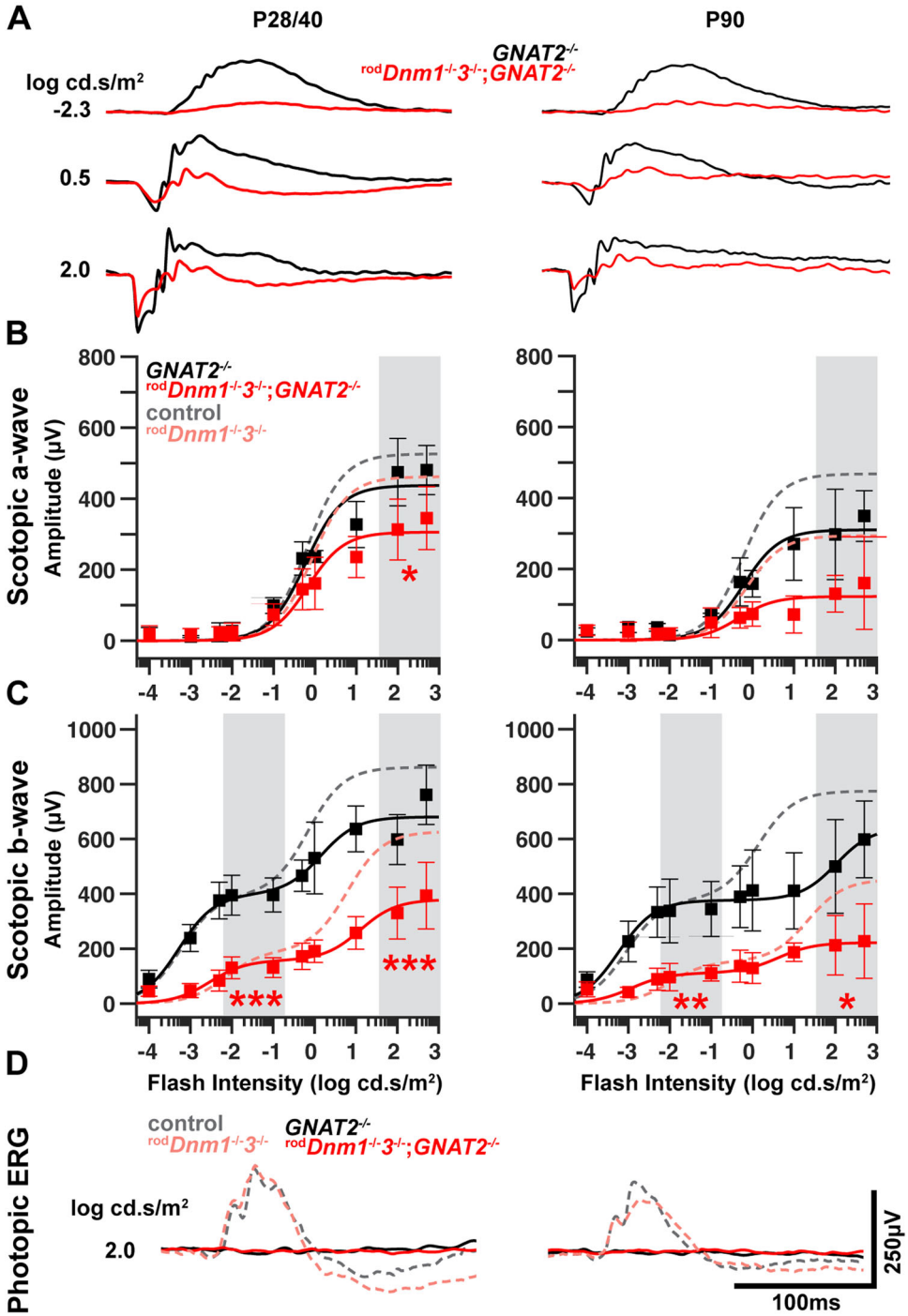

Figure 4. Scotopic ERG responses from *Dnm* double cKO mice lacking cone function (GNAT2$^{-/-}$). Scotopic ERG responses ($n = 4$–9 mice per genotype) from *GNAT2*$^{-/-}$ (black) and ^{rod}*Dnm1*$^{-/-}$/*3*$^{-/-}$;*GNAT2*$^{-/-}$ (red) mice were recorded at P28/P40 and P90 at different single-flash intensities (***A***). The a-wave (***B***) and b-wave amplitudes (***C***) are plotted as a function of increasing flash intensity (mean ± SD). In ^{rod}*Dnm1*$^{-/-}$/*3*$^{-/-}$;*GNAT2*$^{-/-}$ mice (red) at P28/P40, the scotopic a-wave is modestly reduced, whereas the scotopic b-wave is more severely decreased. At P90, the a-wave shows a trend toward impairment ($p = 0.024$), while the b-wave is significantly diminished in *Dnm* double cKO mice. Photopic ERG responses are eliminated in *GNAT2*$^{-/-}$ mice (***D***). Dashed lines in (B) through (D) show comparable data with intact *GNAT2* expression (from Fig. 3). For scotopic responses, comparisons reflect average response over two flash intensities within the gray bars; *$p < 0.01$; **$p < 0.005$; ***$p < 0.0001$.

bipolar cells (RBs), as reflected by the small but persistent b-wave responses to low-intensity flashes below cone threshold (Robson and Frishman, 1998, 2014; Herrmann et al., 2010). To confirm that these weak responses are mediated by rods, we bred the double cKO onto a *Gnat2* (cone transducin) KO background to eliminate cone function (Ronning et al., 2018). On the *Gnat2 KO* background, weak scotopic b-wave responses persisted in the double cKO at both early (P28/P40) and later ages (P90), despite some impairment in the a-wave (Fig. 4*A–C*). For both groups, the *Gnat2* KO background completely eliminated the photopic b-wave, as expected (Fig. 4*D*). These results confirm that rods lacking dynamin 1/3 remain capable of weak synaptic transmission, as reflected by a small, persistent scotopic b-wave.

Dynamins 1 and 3 are not essential for rod survival and outer segment formation

The gradual reduction in the a-wave of the ERG following double cKO of *Dnm1* and *Dnm3* suggests either a loss of phototransduction machinery or a loss of rods. To investigate the functional integrity of rods of $^{rod}Dnm1^{-/-}/3^{-/-}$ mice, we first investigated the localization of rhodopsin in the outer segments. Rhodopsin immunostaining of retinal cross sections performed at P28, P90, and P180 showed its normal localization to the outer segment in both single and double cKO mice (Fig. 5*A,B*; data for single cKO mice are not shown), suggesting that processing of proteins through the biosynthetic membranes (ER—Golgi) and rhodopsin outer segment trafficking pathway persist in the absence of dynamins 1 and 3. Further, the thickness of the ONL, reflecting the number of intact photoreceptors, appeared normal at P28 (Fig. 5*C*), but was reduced slightly in the double cKO mice at P90 (Fig. 5*D*) and reduced further by P180 (Fig. 5*E*). Nevertheless, most (~80%) photoreceptor cells in the double cKO mice survived until P180, and the ONL in single cKO retinas appeared normal at all ages (Fig. 5*C–E*).

Next, we investigated the structure of rod outer segments in single and double cKO mice using TEM at P90 (Fig. 5*F–I*). In these experiments, we used tannic acid instead of osmium tetroxide as a contrast agent to differentiate newly forming "open" discs from mature discs fully enclosed inside the outer segment (Ding et al., 2015). We found that none of the morphological features of outer segments, including the appearance of newly forming discs, of either single or double cKO mice differed from those of control mice (Fig. 5*F–I*). These results show that the outer segment formation, including the process of disc enclosure, does not depend on dynamins 1 and 3.

Dynamins 1 and 3 are essential for the integrity of the rod synaptic ribbon

The reduced scotopic ERG b-wave in $^{rod}Dnm1^{-/-}/3^{-/-}$ mice prompted us to examine the status of their synapses with postsynaptic neurons within the outer plexiform layer. Retinal cross sections from single and double cKO animals were obtained at P28, P90, and P180 and costained with CtBP2, which labels the synaptic ribbon (Maxeiner et al., 2016). WGA, which binds specifically to the matrix surrounding rod photoreceptors, was used to identify postsynaptic neurites from bipolar cells and HCs (Tien et al., 1992; Fig. 6).

The presynaptic CtBP2-labeled ribbons exhibited a rainbow shape in control rods (Fig. 6*A,D,G*), whereas the ribbons in $Dnm1^{-/-}/3^{-/-}$ rods had a reduced length at P28 (Fig. 6*B*) and became punctate at P90 and P180 (Fig. 6*E,H*). We quantified the synaptic ribbon contour length (Fig. 6*C,F,I*) in single and double cKO mice and found a significant reduction in double cKO mice compared with single cKO and control mice. This indicates that dynamins 1 and 3 are essential for the maintenance of the ribbon synapse in rods and that expression of either isoform is sufficient to preserve ribbon integrity.

In control retinas, WGA staining showed postsynaptic neurites that resembled tree branches extending up to and apposing the ribbons (Fig. 6*A,D,G*). These branches appeared shorter and more weakly stained at P90 and P180 in double cKO retinas, although they continued to appose the ribbons, even at P180 as the ribbons retracted into the ONL (Fig. 6*B,E,H*). No changes in WGA staining were observed in single cKO mice at any age (data not shown). We also observed a sustained reduction in the thickness of the outer plexiform layer of the double cKO mice at P90 and P180, likely reflecting severe degeneration of rod synaptic terminals and postsynaptic processes (Fig. 6*E,H*).

Degenerating synapses in $^{rod}Dnm1^{-/-}/3^{-/-}$ rods show reduced expression of ribbon-associated and synaptic vesicle proteins

We made additional assessments of rod synapses of $^{rod}Dnm1^{-/-}/3^{-/-}$ mice by immunohistochemistry using antibodies against ribbon-associated and synaptic vesicle proteins (Fig. 7). First, we stained retinal cross sections of control and double cKO mice for Syt1, a calcium sensor protein localized in presynaptic vesicles (Brose et al., 1992; Chapman et al., 1995; Berntson and Morgans, 2003; Fox and Sanes, 2007). Colabeling with a cone marker, PNA (Blanks and Johnson, 1984), distinguished cone synapses from rod synapses. In control mice, Syt1 is expressed in both rod and cone synaptic terminals (Fig. 7*A*). In double cKO mice, Syt1 labeling of rod synapses was reduced at P28, with further reduction at P90 and P180 (Fig. 7*B*), whereas no obvious changes were observed in single cKO mice (Fig. 7*C,D*). We did not observe changes in the staining of Syt1 in cone synapses of any of the cKO mice. The reduced intensity of Syt1 staining in rods of double cKO mice indicates impaired synaptic transmission in rod synaptic terminals.

Next, we immunostained retinal cross sections with antibodies against bassoon, a scaffolding protein anchoring the ribbon to the active zone (Dick et al., 2003; tom Dieck et al., 2005), and VGluT1, the primary vesicular glutamate transporter in photoreceptors (Johnson et al., 2007; Fig. 7*E,F*). Cones were labeled with an antibody against cone arrestin to identify their synaptic terminals and distinguish them from rod synapses. At P90, when rod synapses degenerated in double cKO retinas, there were losses of bassoon and VGluT1, indicating ribbon disassembly and fewer synaptic vesicles, respectively (Fig. 7*F*). Bassoon-labeled ribbon synapses were rainbow shaped in control retinas (Fig. 7*E*), similar to the staining observed for CtBP2 (Figs. 6, 7*I*). In double cKO mice, rod synaptic ribbons labeled with bassoon and CtBP2 appeared as puncta, and their number was substantially reduced (Figs. 6, 7*E–J*). Lastly, degenerating rod synaptic terminals showed reduced immunostaining of complexin-3, a SNARE complex-associated protein (Reim et al., 2009; Fig. 7*I,J*), consistent with reduced staining of synaptic vesicle markers Syt1 (Fig. 7*B*) and VGluT1 (Fig. 7*F*). In summary, ribbon-associated proteins and synaptic vesicle proteins were severely reduced in rods lacking both dynamins 1 and 3, but neighboring cone synapses remained intact. Deletions of either dynamin 1 or 3 alone in rods displayed no synaptic phenotype (Fig. 7*G,H,K,L*), indicating that either isoform alone is sufficient to maintain the overall integrity of rod synapses.

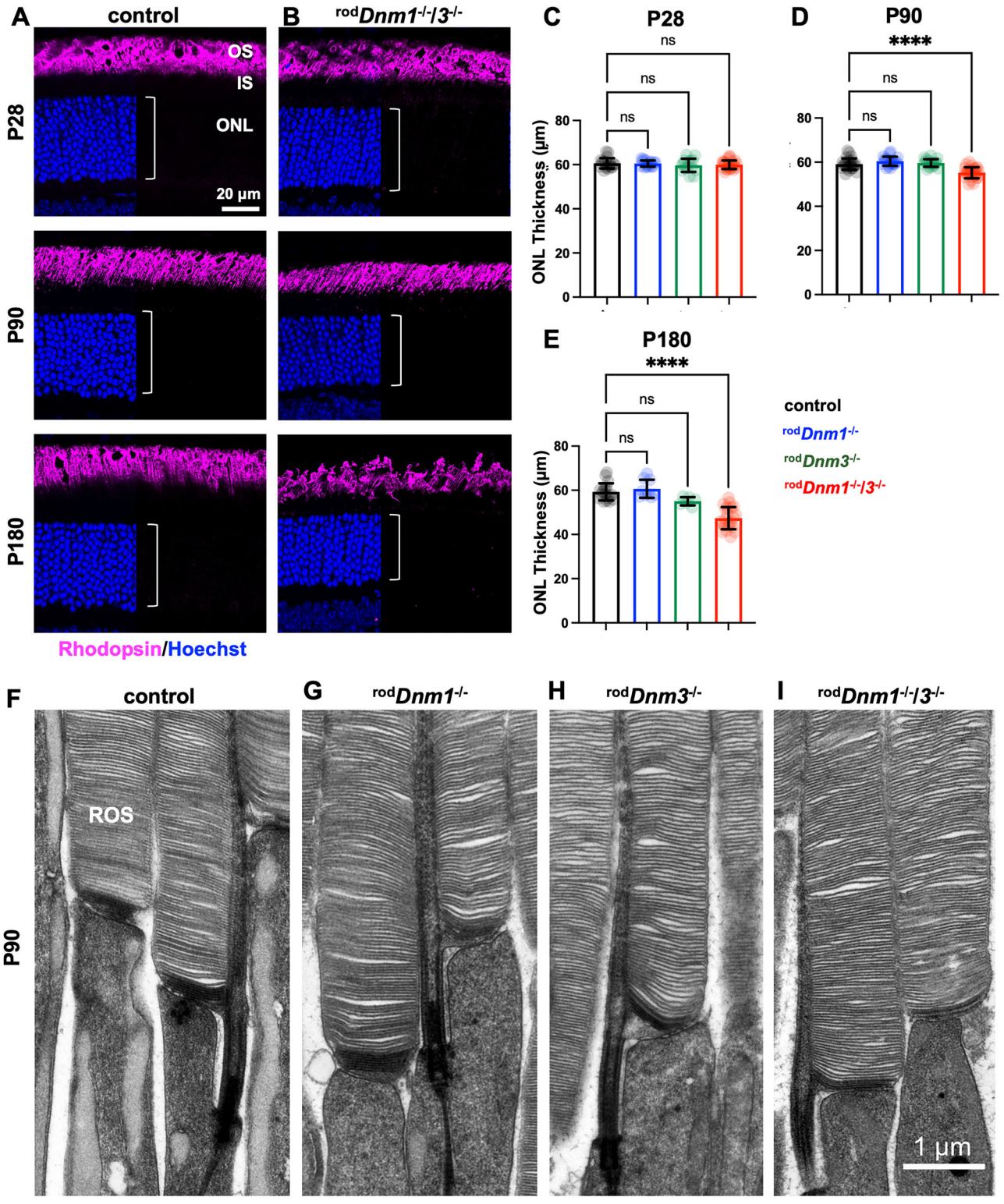

Figure 5. *Dynamin* cKO lines lack an outer segment phenotype. Retinal cross sections of control (***A***) and $^{rod}Dnm1^{-/-}/3^{-/-}$ mice (***B***) obtained at P28, P90, and P180 were stained with an antibody against rhodopsin to label rod outer segments (magenta), and Hoechst staining was used to label photoreceptor nuclei (blue). In all mice, rhodopsin localizes normally to rod outer segments, indicating normal vesicular trafficking from ER to Golgi in the absence of both dynamin isoforms. ***C–E*** The measurements of the ONL thickness in mice of indicated ages and genotypes ($n = 3–5$ mice per condition; mean ± SD). After deletion of dynamins 1 and 3, the ONL thickness is normal at P28 (***C***; control, 60.6 ± 2.4 µm; $^{rod}Dnm1^{-/-}/3^{-/-}$, 60.0 ± 1.9 µm), but is slightly reduced at P90 (***D***; control, 59.1 ± 2.6 µm; $^{rod}Dnm1^{-/-}/3^{-/-}$, 55.2 ± 2.5 µm) and reduced at P180 by ∼20% (***E***; control, 59.3 ± 3.9 µm; $^{rod}Dnm1^{-/-}/3^{-/-}$, 47.4 ± 5.0 µm). ONL thickness in single cKOs is comparable to controls. ****$p < 0.0001$. The ultrastructure of rod outer segments (ROS) assessed by TEM at P90 appears normal in all dynamin cKO lines (***F–I***).

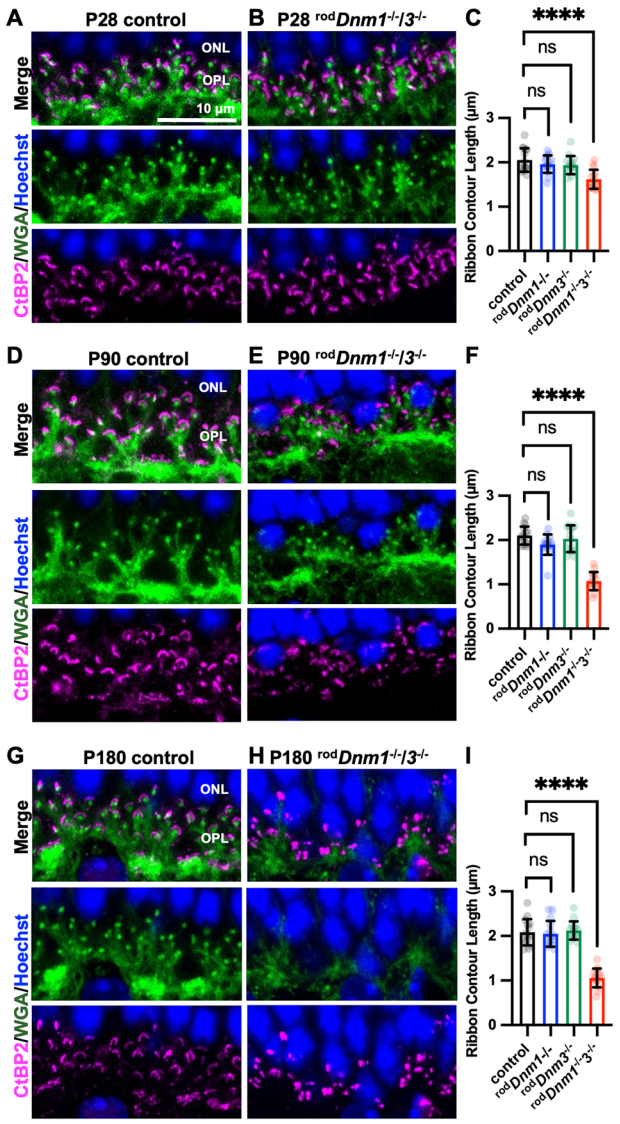

Figure 6. Reduced synaptic ribbon length in *Dnm1/3* double cKO mice. Rod synaptic ribbons and postsynaptic neurites were colabeled with antibodies against CtBP2/RIBEYE (magenta) and WGA (green), respectively. In retinal cross sections from control (***A,D,G***) and $^{rod}Dnm1^{-/-}/3^{-/-}$ mice (***B,E,H***) at P28 (***A–C***), P90 (***D–F***), and P180 (***G–I***), rod synaptic ribbons in double cKO mice are significantly shorter at P28 (***C***; control, 2.1 ± 0.3 µm; $^{rod}Dnm1^{-/-}$, 2.0 ± 0.2 µm; $^{rod}Dnm3^{-/-}$, 1.9 ± 0.2 µm; $^{rod}Dnm1^{-/-}/3^{-/-}$, 1.6 ± 0.2 µm; mean ± SD) and progressively reduce their length at P90 (***F***; control, 2.1 ± 0.2 µm; $^{rod}Dnm1^{-/-}$, 1.9 ± 0.2 µm; $^{rod}Dnm3^{-/-}$, 2.0 ± 0.3 µm; $^{rod}Dnm1^{-/-}/3^{-/-}$, 1.1 ± 0.2 µm) and P180 (***I***; control, 2.1 ± 0.3 µm; $^{rod}Dnm1^{-/-}$, 2.0 ± 0.3 µm; $^{rod}Dnm3^{-/-}$, 2.1 ± 0.2 µm; $^{rod}Dnm1^{-/-}/3^{-/-}$, 1.1 ± 0.2 µm). This reduced length is accompanied by a reduction in the number of identified ribbons in the OPL. The shape and number of synaptic ribbons in rods from single *Dnm* cKOs (***C, F, I***) are comparable to control animals. ****$p < 0.0001$.

Absence of dynamins 1 and 3 at the rod synapse impairs vesicle endocytosis

We performed a more complete investigation of dysfunction of rod synapses lacking dynamins 1 and 3 using TEM to assess synapse ultrastructure (Figs. 8–10). First, we compared the ultrastructure of rods with single and double KO of *Dnm1* and *Dnm3* at P180 (Figs. 8, 9), when the degeneration in double cKO rods should have been obvious and when abnormalities in single cKO (*Dnm1*) or single KO (*Dnm3*) rods, if any, should have been apparent. The germline *Dnm3* KO was used here due to availability of experimental animals.

Rod synapses (Fig. 8*A*) are structurally distinguishable from cone synapses (Fig. 8*B*) based on the smaller size of their axon terminals (Fig. 7*E*) and the presence of a single ribbon associated with one site of invagination; whereas cone synapses have multiple ribbons and sites of invagination as well as obvious basal contacts of multiple bipolar cell dendrites (Mercer and Thoreson, 2011; Thoreson, 2021). The synaptic ribbon is normally intensely stained (long electron-dense area) and anchored to the plasma membrane at the vesicle release site (arciform density, curved electron-dense area); the invaginating neurites from horizontal and bipolar cells have a butterfly shape in cross section in rod and cone terminals (Fig. 8*A,B*). A rod terminal forms an invaginating synapse with the axon terminals of HCs and dendrites of rod bipolar cells (RBs), whereas a cone terminal makes an invaginating synapse with dendrites from HCs and cone bipolar cells (CBs; Burger et al., 2021). In $^{rod}Dnm1^{-/-}/3^{-/-}$ mice at P180, rod synapses severely degenerated: the ribbons appear free floating and disassembling, while the postsynaptic terminals from RBs and HCs were largely absent (Fig. 8*A*, right panel).

Cone terminals in the rod-specific double cKO mice showed well-formed synaptic ribbons that were properly attached to the base, and the invaginating processes from secondary neurons, the HCs and CBs, appeared as a butterfly shape in cross sections at P180 (Fig. 8*B*, right panel). The lack of a phenotype in cones was consistent with the cKO of dynamins 1 and 3 being restricted to rods and shows that cones were not affected for at least 6 months, while nearby rod synapses degenerated, consistent with observations described above (Figs. 3, 6, 7).

Next, we investigated the ultrastructure of the synaptic ribbon in each genotype at higher magnification (Fig. 9). We performed the analysis at P180, when the degeneration in double cKO is advanced and should reveal any changes in single cKO or KO mice as well. In control mice, normal-sized vesicles were located along the ribbon (Fig. 9*Aii*) and filled the cytoplasm of the terminal (Fig. 9*Aiii-iv*). In contrast, double cKO rods contain enlarged endosome-like vesicles (evs) in the cytoplasm and an increased density of Omega profiles (*) reflecting invaginations of the plasma membrane caused by exo- and/or endocytosis (Fig. 9*B*) (Imoto et al., 2022). There was also a loss of the invaginations and a corresponding disassembly of the arciform density. The quantification of vesicle number and size (Fig. 9*E–H*) showed that double cKO rod terminals contained a significantly reduced number of ribbon-associated and cytoplasmic vesicles (Fig. 9*E,G*) and that the ribbon-associated and cytoplasmic vesicles were heterogenous in size, with a larger than normal average diameter (Fig. 9*F,H*). Unlike severely disrupted rod terminals, the neighboring cone terminals in double cKO mice showed synaptic ribbons similar to those in control mice (Fig. 9*C*): in both cases, cone terminals showed normal ribbons attached to the active site with vesicles of normal size and lacked the large evs accumulated in rods (Fig. 9*B,C*).

Single *Dnm1* cKO and *Dnm3* KO rod terminals were qualitatively normal in ultrastructure, with ribbons properly attached to the base and synaptic vesicles appearing homogeneous in size with average diameters similar to controls (Fig. 9*D,F,H*). Quantification of the number of tethered and cytoplasmic vesicles, however, revealed a slight reduction (~15–18%) in the vesicle pool number for *Dnm1* cKO mice, but not for *Dnm3* KO mice (Fig. 9*E,G*). Thus, *Dnm1* cKO rods apparently show a minor phenotype: a slight reduction in synaptic vesicle density apparent at the ultrastructural level.

Lastly, we performed an additional EM analysis from control versus double cKO mice at P40 (Fig. 10). At P40, the ribbons of

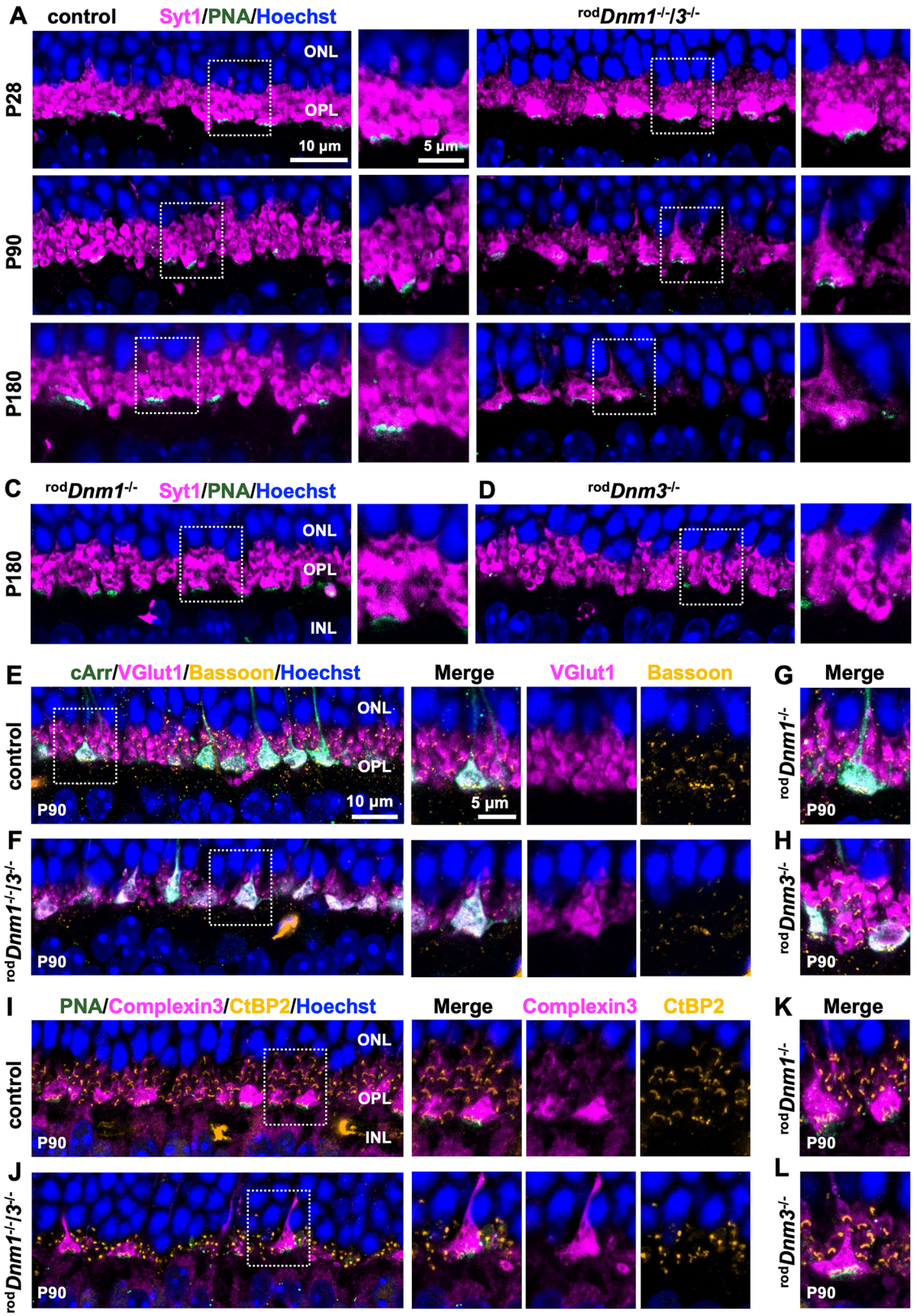

Figure 7. Synaptic proteins are absent in rods after *Dnm1/3* cKO. Immunostaining of retinal cross sections from control (***A***) and $^{rod}Dnm1^{-/-}/3^{-/-}$ mice (***B***) with an antibody against Syt1 (magenta) shows severe reduction in the Syt1 staining in double cKO rods at P28, which is followed by severe degeneration of rod synapses at P90 and P180; cones, labeled with PNA (green), show normal intensity of Syt1 staining in double cKO retinas. In $^{rod}Dnm1^{-/-}$ (***C***) and $^{rod}Dnm3^{-/-}$ (***D***) retinas at P180, Syt1 staining of rods and cones resembles the staining in control retinas (***A***). At P90, retinal cross sections from control (***E, I***), $^{rod}Dnm1^{-/-}$ (***G, K***), $^{rod}Dnm3^{-/-}$ (***H, L***), and $^{rod}Dnm1^{-/-}/3^{-/-}$ mice (***F, J***) were stained for synaptic vesicle proteins (***E–H***, vesicular glutamate transporter 1, VGluT1, magenta; ***I–L***, complexin 3, magenta) and ribbon-associated proteins (***E–H***, bassoon, yellow; ***I–L***, CtBP2, yellow). Only in double cKO retinas (***F, J***) the staining of these marker proteins is significantly reduced, indicating impaired synaptic vesicle machinery in rods. Immunostaining of single cKO retinas resembles that in control mice. Cone synapses are labeled with antibodies against cone arrestin (cArr, ***E–H***) and PNA (***I–L***).

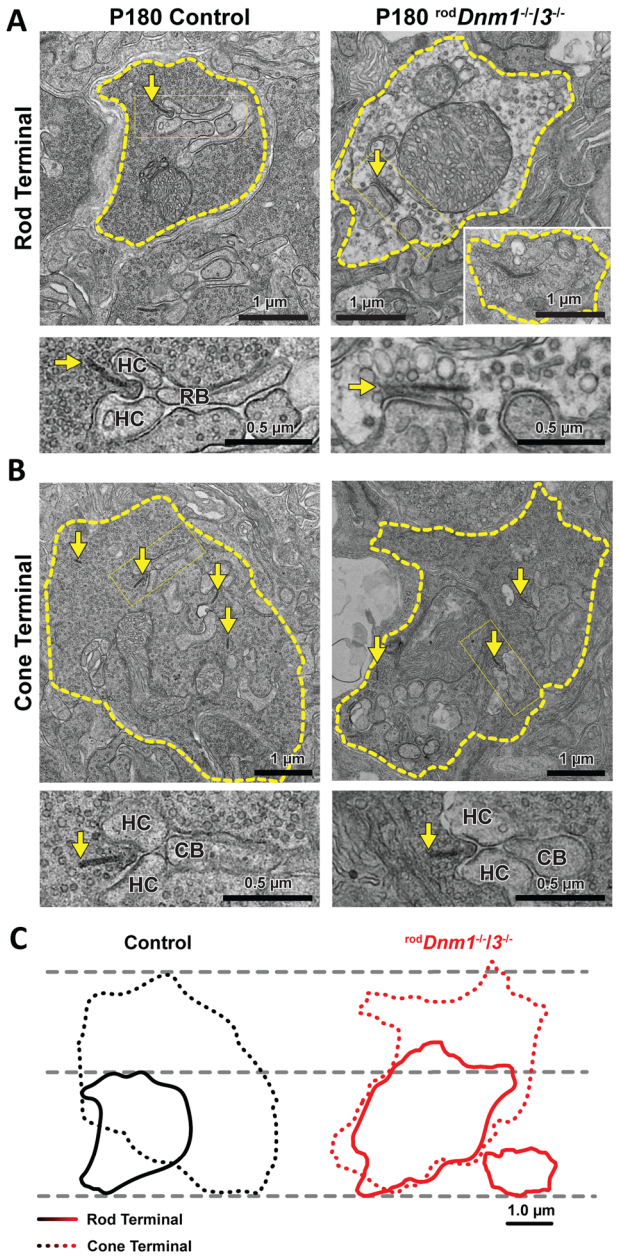

Figure 8. Rod synapses severely degenerated in rods lacking *Dnm1* and *Dnm3*. Ultrastructural analysis of rod (***A***) and cone synaptic terminals (***B***) from control (left panels) and $^{rod}Dnm1^{-/-}/3^{-/-}$ (right panels) mice at P180. ***A***, Rod synaptic terminals in control mice have one ribbon (yellow arrow) and form an invaginating synapse with HC axon terminals and RB dendrites; see enlargements for details. ***B***, Cone synaptic terminals are generally larger, contain multiple ribbons (yellow arrows) and invagination sites, and are formed with HC and CB dendrites; see enlargements for details. In dynamin double cKO mice, the rod terminal (two examples shown) contains a detached ribbon, and the invagination site is degenerating (***A***), whereas the neighboring cone synapses remain intact and are structurally comparable to those in control mice (***B***). ***C***, Relative sizes of the example terminals shown in (***A,C***).

double cKO rods were fully formed (Fig. 10*B*), as in control rods (Fig. 10*A*), and attached near invaginating postsynaptic terminals. The rod terminals in double cKO retinas, though, contained enlarged evs in the cytoplasm (Fig. 10*B*). A defect in dynamin-dependent endocytosis caused accumulation of Omega-shaped profiles across the plasma membrane, and the arciform structure at the base of the ribbon was nearly absent along with flattening of the active zone. Further, the density of both ribbon-associated and cytoplasmic synaptic vesicles (Fig. 10*C,E*) was reduced, and the vesicle pool was more heterogeneous in size with an increased average diameter (Fig. 10*D,F*). These data show that, in the absence of dynamins 1 and 3, synaptic vesicle endocytosis is impaired leading to a reduced density of synaptic vesicles and an increase in vesicle diameter, already by P40, along with a progressive degeneration of the rod synapse.

Rod bipolar cell dendrites degenerate in $^{rod}Dnm1^{-/-}/3^{-/-}$ retinas

We investigated the impact of presynaptic degeneration on postsynaptic neurons, starting with RB dendrites, in the $^{rod}Dnm1^{-/-}/3^{-/-}$ mice. RBs were labeled in retinal cross sections with an antibody against protein kinase C-alpha (PKCα; Huh et al., 2015; Keeley et al., 2022). Glutamate receptors at the ON bipolar cell dendrites, including those of RBs, were labeled with an antibody against metabotropic glutamate receptor 6 (mGluR6; Masu et al., 1995; Cao et al., 2009, 2011; Fig. 11). At P28, mGluR6 was normally expressed at the tips of postsynaptic terminals of bipolar cells of double cKO rods (Fig. 11*A*). At P90, when the rod synapse is progressively degenerating, we observed a reduced expression of mGluR6 at the postsynaptic terminals of RBs. While most of their dendrites degenerated, a few extended into the ONL (Fig. 11*B*). At P180, expression of mGluR6 was reduced further, and most RBs obviously degenerated (Fig. 11*C*).

We next imaged retinal flat mounts from control and double cKO retinas to evaluate overall sprouting of the RB dendrites into the outer plexiform layer (Fig. 11*D,E*). Staining double cKO retinas with an anti-PKCα antibody identified uniform sprouting of RBs' postsynaptic terminals into the outer plexiform layer at P28, which was substantially reduced at P90 and almost absent at P180 (Fig. 11*E*). Despite the lack of dendrites, the number of RBs at P180, quantified by the density of PKCα-labeled somas in flat mounts, was similar in control ($14{,}006 \pm 1{,}963$ cells/mm^2) and double cKO retinas ($14{,}488 \pm 628$ cells/mm^2) and matched the reported density (Hovhannisyan et al., 2015; Kautzman et al., 2018; Keeley et al., 2022).

The effect of dynamin 1/3 deletion in rods on RB dendrites was characterized additionally by costaining RBs for PKCα and presynaptic sites for bassoon (Fig. 11*F,G*). Comparing control and dynamin double cKO retinas, PKCα-labeled dendrites sprouted toward the bassoon-labeled base of the photoreceptor synaptic ribbon at P28, whereas these structures are reduced in double cKO retinas at P90 and essentially absent at P180 (Fig. 11*F,G*). No phenotype was observed in single cKO mice (data not shown). Notably, the reduction in bassoon staining in the double cKO retina at P180 was more substantial than the reduction in staining of the ribbon (CtBP2; Fig. 6*H*). Taken together, these data indicate that the degeneration of the double cKO rod synaptic terminal causes the subsequent degeneration of RB dendrites.

HC axon terminals degenerate in $^{rod}Dnm1^{-/-}/3^{-/-}$ retinas

Because the degeneration of rod synapses in the $^{rod}Dnm1^{-/-}/3^{-/-}$ retina causes the loss of RB dendrites, we also investigated postsynaptic processes of the HCs (Fig. 12). In retinal cross sections, HCs were labeled with an antibody against calbindin-1 (Pasteels et al., 1990; Peichl and Gonzalez-Soriano, 1994), and their axon terminals were labeled with an antibody against Syt2/ZNP-1; Syt2/ZNP-1 also labels Type 2 OFF CBs as well as the axon terminals of Type 6 ON CBs (Fox and Sanes, 2007; Wassle et al.,

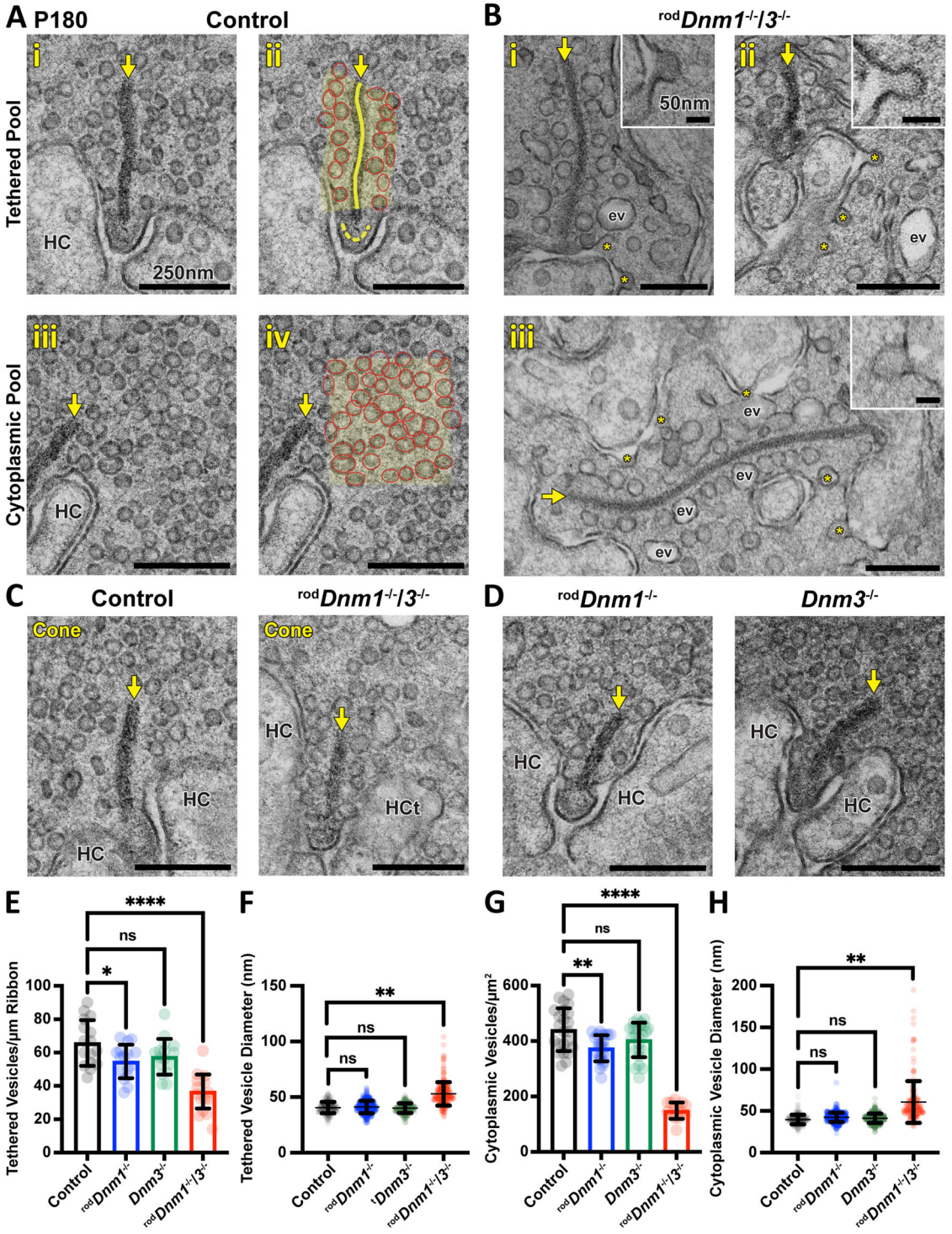

Figure 9. Lack of dynamin 1/3-dependent endocytosis in rod synaptic terminals causes formation of enlarged endosome-like vesicles and Omega profiles. The ultrastructure of rod (***A, B, D***) and cone (***C***) synaptic ribbons was assessed by TEM in control (***A, C***), *Dnm1/3* cKO (***B, C***), and *Dnm1* cKO and *Dnm3* KO mice (***D***) at P180. The synaptic ribbon (yellow arrow) is intensively stained and attached to the membrane at its base (arciform density, dashed yellow line, ***Aii***). Control synapses contain a homogeneous pool of tethered and cytoplasmic vesicles: the tethered pool (red ellipses, ***Aii***) are within 100 nm of the ribbon (shaded yellow area surrounding the yellow line, ***Aii***), and the cytoplasmic pool (red ellipses within yellow shaded area, ***Aiv***) are free floating in the cytoplasm. ***B***, In double cKO mice, vesicles are heterogenous in size and enlarged (evs); impaired vesicle endocytosis halts vesicle release from the plasma membrane resulting in the formation of Omega profiles (*; ***Bi–iii***). Ultrastructure from cone ribbon synapses appears similar in double cKO mice and control mice (***C***). The cone pedicles remain intact, with multiple ribbons attached to invagination sites and a homogenous pool of normal-sized vesicles present in the cytoplasm, without signs of enlarged evs. Rod ribbon synapses from single cKO/KO mice (***D***) appear relatively normal with a homogeneous pool of vesicles. ***E–H***, Quantification of the number (***E, G***) and size (***F, H***) of the tethered (***Aii***, ***E, F***) and cytoplasmic vesicle pools (***Aiv***, ***G, H***) in control, single cKO/KO, and double cKO mice at P180 (mean ± SD). ***E–H***, Double cKO mice have a significant reduction in the vesicle number and form larger vesicles, whereas *Dnm3* KO (green) are indistinguishable from controls (black); at this age, *Dnm1* cKO (blue) show a moderate reduction in vesicle number for both tethered (18.1%) and cytoplasmic pools (15.2%), but no change in vesicle size. *$p < 0.05$; **$p < 0.01$; ****$p < 0.0001$.

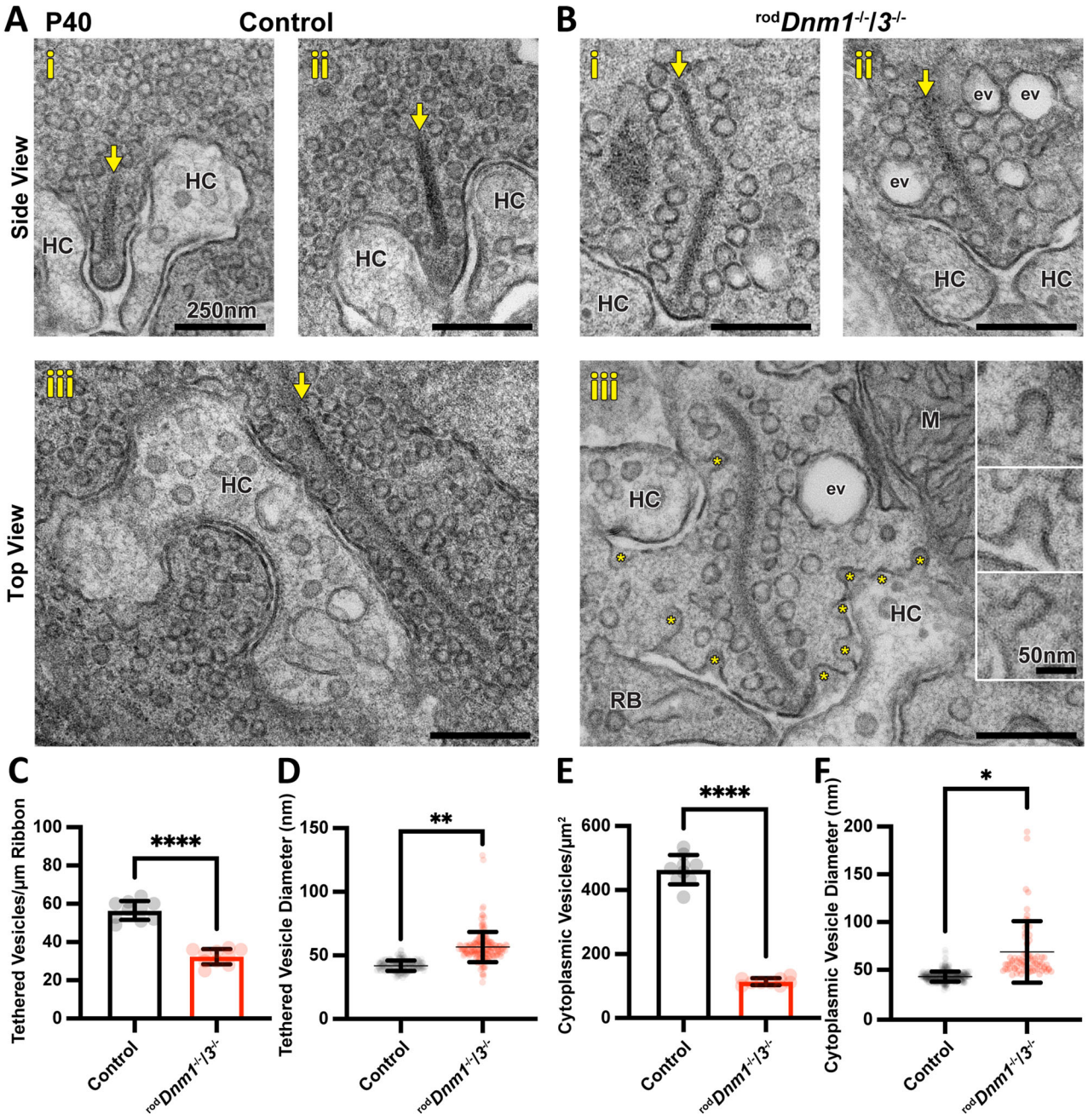

Figure 10. Dynamin-dependent endocytosis is impaired in rod synapses lacking dynamin 1/3 at P40. Ultrastructure from control (***A***) and $^{rod}Dnm1^{-/-}/3^{-/-}$ retinas (***B***) was performed at P40, when the rod synaptic terminals start to degenerate in double cKO mice. Ultrastructure is shown from side (***i-ii***: upper panel) and top views (***iii***: lower panels). In the absence of dynamin-dependent endocytosis, enlarged evs and Omega profiles (*) develop along the plasma membrane of double cKO rod synapses (***B***); see enlargements for details. The processes from the invaginating horizontal axon terminals in control and double cKO rod synapses are indicated as HC. M, mitochondria. ***C–F***, Quantification of tethered (***C, D***) and cytoplasmic (***E, F***) vesicle pools in control (black) and double cKO (red) mice (mean ± SD): in the absence of dynamin 1/3, the number of vesicles is significantly reduced in both pools (***C, E***), and the size of the tethered and cytoplasmic vesicles is significantly enlarged (***D, F***). *$p < 0.05$; **$p < 0.01$; ****$p < 0.0001$.

2009; Fig. 12*A–F*). In control retinas, HCs were stained for calbindin-1, and their axon terminals, which sprout into the outer plexiform player, were stained for Syt2/ZNP-1 (Fig. 12*A–C*). In double cKO retinas, HCs displayed a normal pattern of calbindin-1 staining at P28, but their Syt2-labeled axon terminals showed a mild degeneration (Fig. 12*D*). This degeneration progressed, such that most of the Syt2-labeled terminals were gone at P90 (Fig. 12*E*), and they were nearly eliminated at P180 (Fig. 12*F*). The calbindin-1 staining was also reduced at the later ages.

We confirmed these findings in retinal flat mounts and found no change in the density of calbindin-1-stained HCs in control and double cKO at P28, P90, and P180 (Fig. 12*G–L*, left panels). Calbindin-1-labeled somas had similar density in control (1,010 ± 86 cells/mm^2) and double cKO retinas (1,101 ± 111 cells/mm^2) at P180 and matched the reported density (Jeon et al., 1998; Hovhannisyan et al., 2015). In contrast, we found progressive reduction in neurite sprouting of Syt2-labeled HC axon terminals in the double cKO, as early as P28 (Fig. 12*G–L*, right panels); the staining for Syt2/ZNP-1 reduced further at P90 and P180

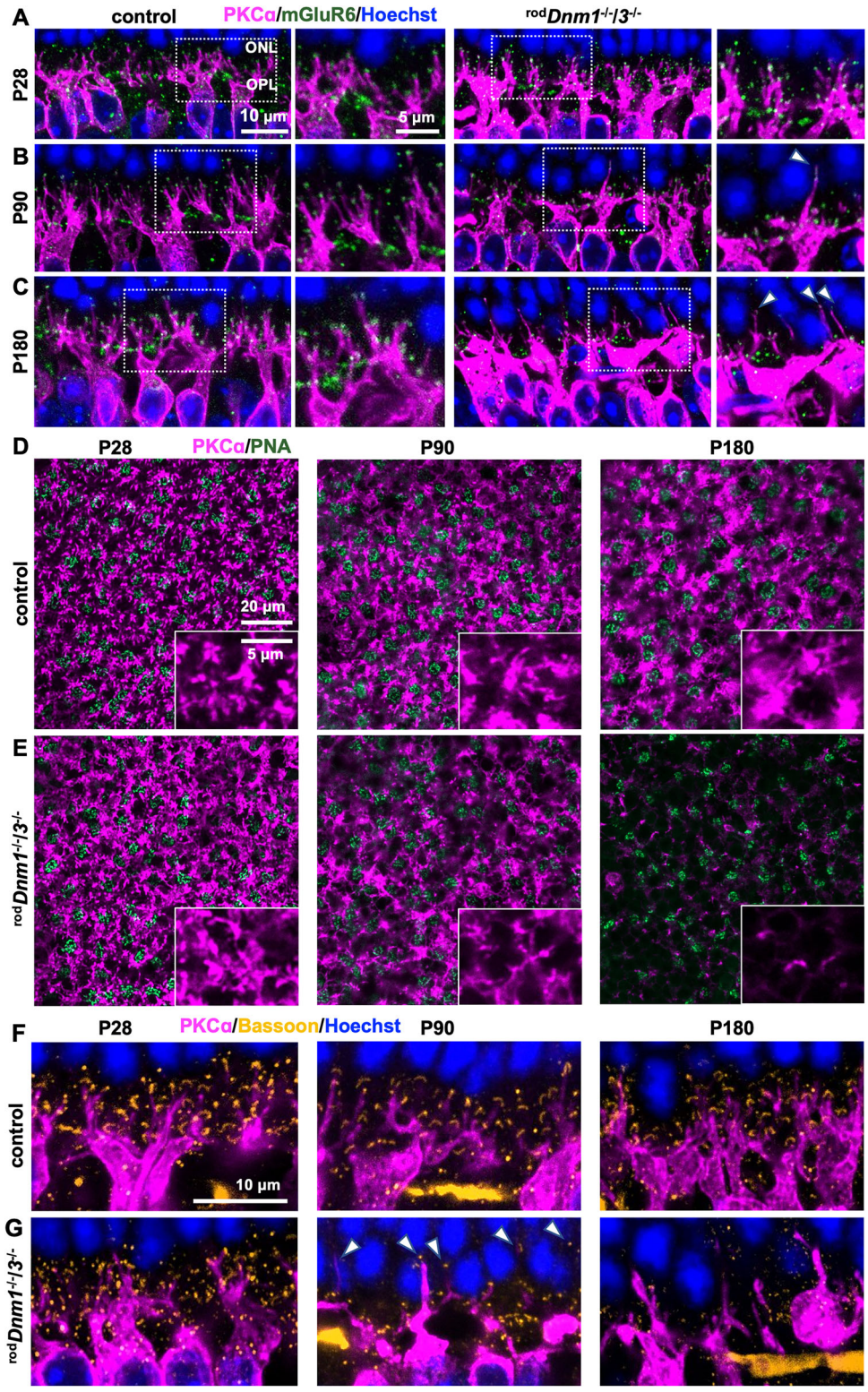

Figure 11. RB dendrites disassemble in dynamin double cKO mice. RB dendrites in retinal cross sections obtained at P28 (***A***), P90 (***B***), and P180 (***C***) were costained with antibodies against PKCα (magenta) and mGluR6 (green). In control mice (***A–C***; left panels), RB dendrites sprout normally into the outer plexiform layer expressing mGluR6 at their postsynaptic terminals. After *Dnm1/3* cKO in rods, RB dendrites sprout with normal mGluR6 expression at P28 (***A***; right panels), indistinguishable from control mice, but later undergo progressive degeneration at P90 and P180 with some dendrites extending into the ONL (indicated with white arrowheads; ***B, C***; right panels). This degeneration of RB dendrites is accompanied by reduced staining of mGluR6 at their postsynaptic terminals. Enlarged images are shown to the right of each panel. Progressive degeneration of RB dendrites is also shown in retinal flat mounts, in which the dendrites are stained with anti-PKCα antibody (magenta). PNA marking cone terminals (green) was used to identify normal Z-projections of RB dendrites between the ONL and the outer plexiform layer (***D, E***). Enlarged images are shown to the right of each panel. Staining of retinal cross sections for the presynaptic protein bassoon (yellow) and the RB marker, PKCα (magenta), shows progressive loss of RB dendrites in $^{rod}Dnm1^{-/-}/3^{-/-}$ retinas and the disintegration of their synaptic connections with rods (***F, G***). Staining intensity for bassoon becomes progressively reduced at P90 and P180 in the double cKO retina (***G***) compared with the control (***F***), indicating dynamin is required for the maintenance of the rod synaptic terminal.

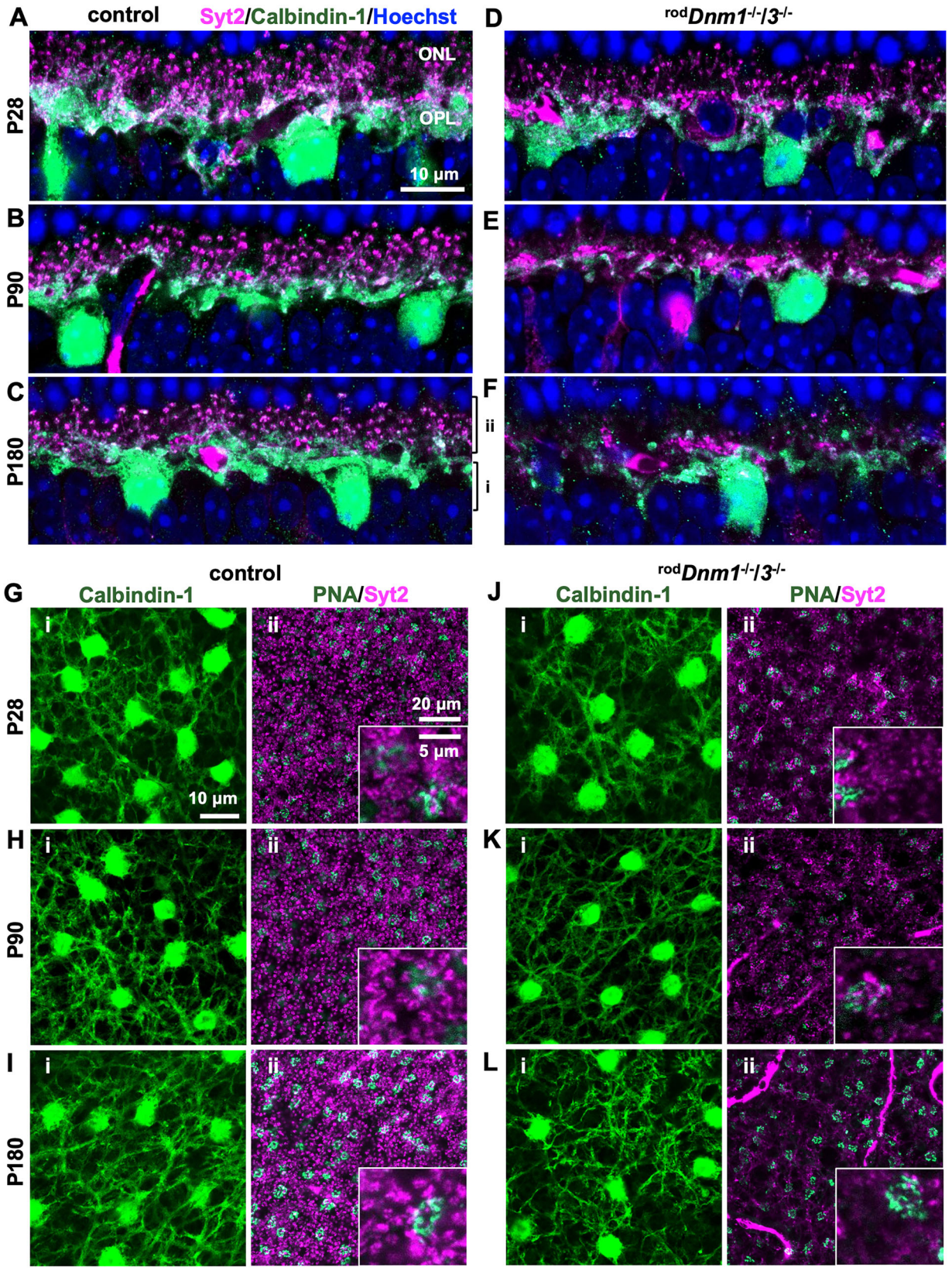

Figure 12. Horizontal cell axon terminals degenerate in dynamin double cKO retinas. The structure of HCs in control and $^{rod}Dnm1^{-/-}/3^{-/-}$ retina was evaluated in retinal cross sections (***A–F***) and flat mounts (***G–L***) at P28, P90, and P180. HCs were stained for their marker calbindin-1 (green), and their axon terminals were labeled with an antibody against Syt2/ZNP-1 (magenta). In cross sections, HC bodies are visible at all ages; however, their axon terminals progressively degenerate: reduced staining for Syt2/ZNP-1 indicates that the degeneration starts at P28 (***D***) and progresses at P90 (***E***) and P180 (***F***); at P180, most axon terminals are gone. The remaining staining in (***F***) most likely originates from synaptic connections between cones and HC dendrites. Retinal flat mounts, stained for calbindin-1 (green; i: left panels) and Syt1/ZNP-1 (magenta; ii: right panels), confirmed that HC axon terminals start to degenerate at P28 (***G, J***) and continue degenerating at P90 (***H, K***) and P180 (***I, L***). PNA colabeling (green) in the right panels (ii) identified the layer connecting cone photoreceptor synapses with HCs. Enlargements are shown for details.

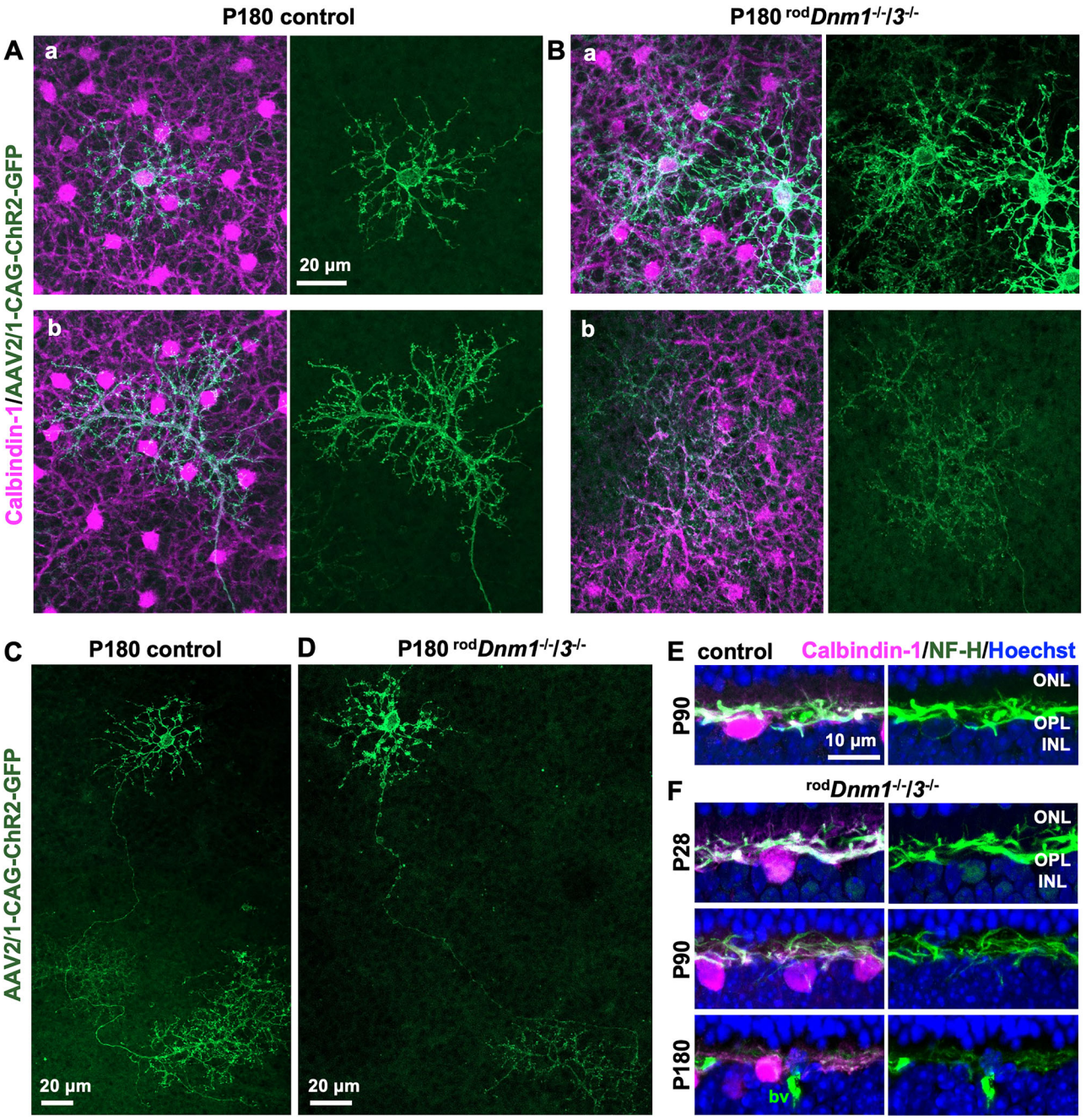

Figure 13. HC somas and dendrites remain intact in dynamin double cKO retinas. Intravitreal injection of AAV2/1-CAG-ChR2-GFP was used to sparsely label HCs (green), which were costained for their marker calbindin-1 (magenta; ***A–F***). Representative images from control (***A, B, E***) and double cKO mice (***C, D, F***) are shown at P180: somas with dendrites appear normal in both cases (***A, C***), whereas the axon in double cKO severely degenerated and is barely visible. Whole AAV-transfected HC from control and double cKO mice are shown in ***E*** and ***F***, respectively. Staining of retinal cross sections from control (***G***) and double cKO (***H***) mice with an antibody against a neurofilament (NF-H) shows the progressive degeneration of the axon terminal (***H***). The axon colocalizes with calbindin-1 staining at P28 (***H***, upper panel), but the staining intensity of both markers progressively decreases with age; only calbindin-1-labeled somas are intensively stained in double cKO mice at P180 (***H***, lower panel). bv, blood vessel.

(Fig. 12*J–L*, right panels). Taken together, the axon terminals of HCs degenerate simultaneously with rod synapses, but the HCs survive and maintain dendritic contacts with cone terminals. It also appears that the HC axon terminals degenerate faster than the RBs (Fig. 12).

Two additional experiments suggested that HC axon terminals degenerate in the double cKO retina. First, we labeled HCs sparsely using AAV-mediated infection (AAV2/1-CAG-ChR2-GFP; see Materials and Methods) and analyzed them at P180. In control retinas, both dendritic and axonal compartments were intact (Fig. 13*A–C*), whereas in double cKO retinas, the axonal compartment showed severe signs of degeneration (Fig. 13*A, B,D*). Second, we stained axon terminals of HCs with an antibody against a neurofilament (NF-H) protein (Peichl and Gonzalez-Soriano, 1993, 1994). We found a progressive and severe reduction in the staining intensity for the neurofilament in the double cKO retina (Fig. 13*F*) compared with control (Fig. 13*E*). Collectively, our results show that, whereas deletion of dynamins 1 and 3 from rods does not affect the ability of HCs to survive and maintain dendritic connections to cone terminals, their axon

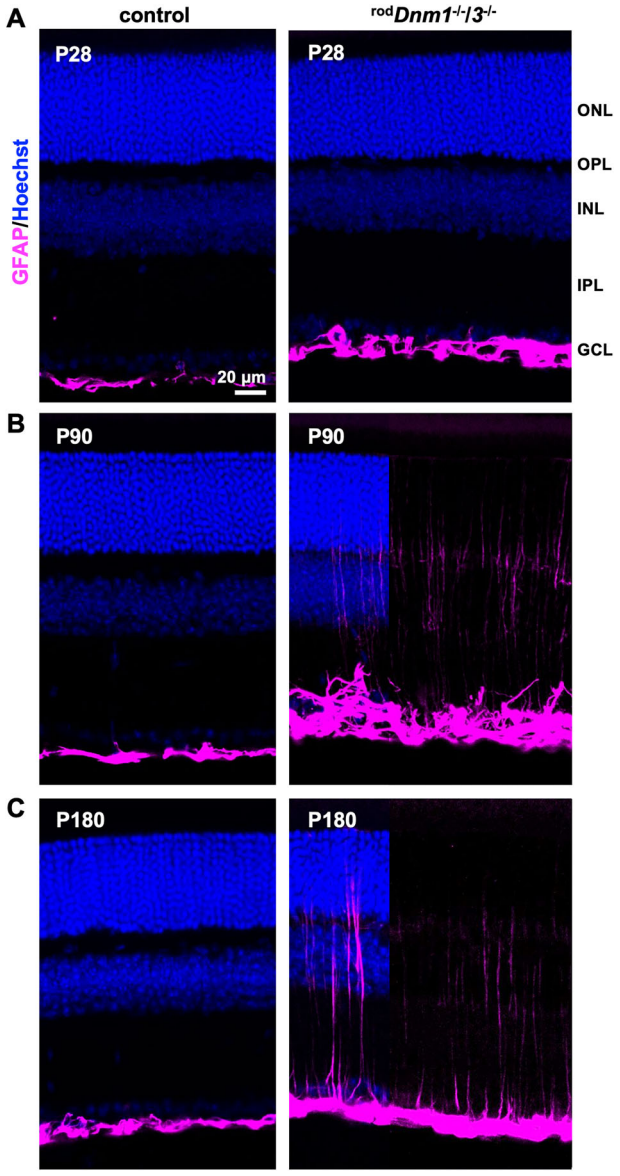

Figure 14. Müller glia cells become stressed in dynamin double cKO mice. Retinal cross sections from control and dynamin double cKO mice were stained for GFAP, a marker identifying astrocytes and Müller glia cells (magenta). In control retina, GFAP staining was confined to astrocytes on the retinal surface. Staining of this area was more extensive in the double cKO retina at P28 (***A***) and spread toward the ONL at P90 (***B***) and P180 (***C***), indicating activation of Müller glia.

terminals progressively degenerate along with the rod terminals (Figs. 12, 13).

Degeneration of rod terminals stresses the retina

To evaluate the presence of increased stress in the double cKO retina, we immunostained for GFAP, which labels astrocytes and activated Müller glial cells (Eisenfeld et al., 1984; Paisley and Kay, 2021; Fig. 14). Control retinas displayed characteristic staining on the vitreous surface of the retina at all ages, which reflects the normal labeling of astrocytes. By contrast, double cKO retinas displayed enhanced staining around the ganglion cell layer at P28, which extended to the ONL at P90 and P180 (Fig. 14*B*,*C*). This staining pattern reflects progressive labeling of Müller cells and indicates increased stress and inflammation over time (Yang et al., 2015).

Discussion

Conditional deletion of the neuronal dynamins 1 and 3 in rod photoreceptors showed that the two isoforms act redundantly to maintain the function of rod synapses. Indeed, no obvious phenotype was observed after deleting *Dnm3*, and only a modest (~15–18%) reduction in synaptic vesicle density was observed after deleting *Dnm1*, with no detectable functional deficiency. By contrast, deleting both isoforms caused progressive degeneration of rod synapses and severely impaired synaptic transmission between rods and RBs. Structural degeneration of rod terminals —including reduced ribbon length, synaptic vesicle density, and enlarged vesicles—was evident at P28, when rod phototransduction remained intact, and progressed until P180. As rods degenerated, RBs retracted most dendrites while extending others toward the ONL, particularly at P90 and P180. HC axon terminals started retracting at P28, yet their dendrites retained connections with cone terminals. Müller glial cells became reactive by P90, presumably in response to the degeneration of rod terminals and postsynaptic processes. Interestingly, rods did not degenerate entirely, and they continued to express rhodopsin in their outer segments. Cones remained intact and functional despite their gap junction coupling to rods (Ishibashi et al., 2022). Collectively, our results establish dynamins 1 and 3 as essential components of synaptic vesicle endocytosis at rod synaptic terminals and illustrate the importance of intact endocytosis for the structural and functional integrity of rod ribbon synapses and their downstream circuits (Fig. 15).

A redundant role for dynamin isoforms in rod ribbon synapse function

In conventional neurons, the function of dynamins 1 and 3 partially (cortical cells) or totally (globular bushy cells) overlaps, such that deleting both isoforms is required to severely disrupt synaptic transmission (Ferguson et al., 2007; Raimondi et al., 2011) and synaptic development (Fan et al., 2016). Our results support similar redundancy in dynamin 1 and 3 function at rod ribbon synapses, at which either isoform alone supported rod synaptic function in dark-adapted conditions when the release rate should be maximal. This is surprising, as vesicle cycling in support of high release rates can depend strongly on dynamin 1 at conventional synapses (Ferguson et al., 2007; Lou et al., 2008; Ferguson and De Camilli, 2012; Shi et al., 2022).

Surprisingly, the only deficit we found in the *Dnm1* KO was a modest (~15–18%) reduction in synaptic vesicle density, which was not associated with a reduced scotopic b-wave. The scotopic ERG may lack sufficient sensitivity to measure functional changes associated with a small change in presynaptic vesicle density, due to postsynaptic saturation of the mGluR6-mediated signaling cascade in RBs (van Rossum and Smith, 1998; Field and Rieke, 2002; Sampath and Rieke, 2004). More refined measures of synapse function may be required to detect a functional defect following *Dnm1* deletion from rods (Sheng et al., 2007; Grabner et al., 2016, 2023; Grabner and Moser, 2021).

Just as surprising was our finding of continued, albeit severely reduced, functionality of the rod synapse in double cKO mice. Despite the conditional deletion of dynamins 1 and 3, and the apparent lack of protein expression by P28, the rod synapse continued to function at a reduced level, as reflected by a weak but persistent scotopic b-wave at flash intensities below ~0.05 ($-1.3\ \log_{10}$) cd/s/m^2 at which cones do not contribute to ERG responses (Robson and Frishman, 1998,

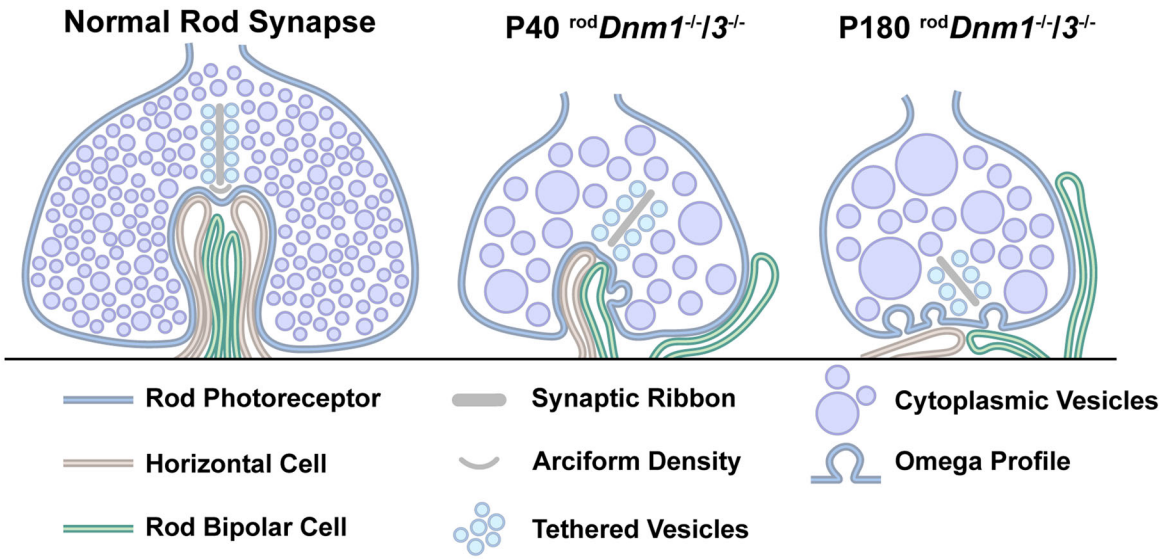

Figure 15. *Dnm1/Dnm3* deletion in rods impairs synaptic vesicle endocytosis and causes progressive degeneration of ribbon synapses. A normal rod synapse is filled with synaptic vesicles homogeneous in size; it has a single synaptic ribbon tethered with vesicles attached; and it forms one invagination site for the synaptic vesicle release of the neurotransmitter glutamate to HC axon terminals and RB dendrites (left illustration). In the absence of dynamins 1 and 3 at P40, enlarged evs in the cytoplasm and Omega profiles along the plasma membrane start forming; processes from HCs and rod bipolar cells retract from the invagination site; and the ribbon attached to the slowly disappearing vesicle release site becomes shorter (middle illustration). A more severe phenotype is observed by P180: enlarged evs accumulate in the cytoplasm, the synaptic ribbon detaches from the active site, HC axon terminals degenerate, and RB dendrites either retract or extend into the ONL (right illustration).

2014; Herrmann et al., 2010). At P180, there is major degeneration of the rod terminal as well as postsynaptic RB dendrites. Still, these dendrites extend toward retracting rod terminals and must continue to make synapses, albeit with reduced expression of mGluR6. This weak synaptic transmission would apparently require a dynamin 1/3-independent mechanism for recycling the remaining synaptic vesicles. This could be mediated by dynamin 2, although it is expressed only minimally in neurons, and its overexpression did not compensate for dynamin 1/3 KO in cortical neurons (Ferguson et al., 2007; Raimondi et al., 2011) or hippocampal neurons (Imoto et al., 2022). There may be dynamin-independent mechanisms that operate at the rod synapse, involving a stage of bulk endocytosis, prior to the formation of synaptic vesicles, consistent with endosomes observed in degenerating rod terminals (Xu et al., 2008; Wahl et al., 2013; Wu et al., 2014). This would imply at least two modes of endocytosis at the rod synapse (Jockusch et al., 2005; LoGiudice and Matthews, 2007; Logiudice et al., 2009; Fuchs et al., 2014; Kesharwani et al., 2021).

Time course of impaired endocytosis and synapse degeneration following loss of dynamin

Disrupted synaptic vesicle endocytosis at P28 in rod terminals was followed by more severe degeneration at P90 and P180, suggesting that impaired endocytosis precedes—and may cause—synapse degeneration. Impaired endocytosis also could disrupt the active zone, which otherwise would remove extraneous synaptic proteins through routine membrane recycling (Neher, 2010). The lack of recycling could disperse voltage-gated Ca^{2+} channels, which could perturb exocytosis further (Wen et al., 2018).

Impact of dynamin deletion on the rod photoresponse

Despite the degeneration of rod synapses following *Dnm1/3* cKO, the rods mostly survived, retained outer segments, and exhibited normal rhodopsin localization. The scotopic a-wave, however, declined at P90/P180, possibly owing to the ∼20% reduction in rods. The degeneration of rod terminals in the double cKO could reduce the circulating current that underlies the a-wave, although this would presumably be a modest effect (Robson and Frishman, 2014), and retraction of rod terminals may not reduce the a-wave (Sanuki et al., 2015). A mild impairment of the a-wave, accompanied by a more severe disruption of the b-wave, occurred after perturbing L-type Ca^{2+} channel signaling (Haeseleer et al., 2004; Mansergh et al., 2005; Kerov et al., 2018). Thus, the reduced a-wave shown here might be explained by some combination of cell loss, disrupting Ca^{2+} channels and altered phototransduction.

Disassembly of postsynaptic processes following degeneration of rod synapses

Deletion of proteins necessary for synaptic transmission usually causes retraction of rod terminals and extension of both RB dendrites and HC axon terminals into the ONL (Burger et al., 2021). Examples include KO of the Ca channel subunit Cacna1f (Mansergh et al., 2005; Chang et al., 2006), the auxiliary Ca channel subunit Cacnα2δ4 (Wang et al., 2017; Kerov et al., 2018), Ca^{2+}-binding protein 4 (CaBP4; Haeseleer et al., 2004), and the scaffolding proteins bassoon (Dick et al., 2003; tom Dieck et al., 2005; Specht et al., 2007), CAST (tom Dieck et al., 2012), and 4.1G (Sanuki et al., 2015). A similar phenotype was observed after knocking out either the serine/threonine kinase LKB1 or one of its targets, AMPK (Samuel et al., 2014), and it occurred in aged wild-type mice, too (Samuel et al., 2011).

In other cases, rod terminals and RB dendrites remain intact, and HC axon terminals alone extend into the ONL: for example, following KO of the ribbon scaffolding protein RIBEYE (Maxeiner et al., 2016) and the cell adhesion molecule SynCAM1 (Ribic et al., 2014). However, in none of these cases did RB dendrites extend into the ONL while HC axons degenerated, as we observed (Fig. 15). Thus, impaired endocytosis following dynamin 1/3 deletion in rods apparently prevents

maintenance of HC connections to rods, leading to HC axon terminal degeneration.

Potential role of dynamin at other ribbon synapses in the retina

We found that dynamins 1 and 3 together are required to maintain the function of mouse rod synapses, which is consistent with the apparent dynamin dependence of endocytosis in salamander (Van Hook and Thoreson, 2012) and mouse rods (Wahl et al., 2013) revealed in pharmacological studies using the dynamin inhibitor dynasore and a nonhydrolyzable GTP analog (GTPγS). Endocytosis and the role(s) of dynamins at other retinal ribbon synapses, however, may differ: endocytosis in salamander cones appears to be unaffected by dynasore and intracellular injections of GTPγS, suggesting a distinct dynamin-independent mechanism for endocytosis (Van Hook and Thoreson, 2012).

Further, studies of bipolar cell synapses have yielded inconsistent findings of dynamin function: endocytosis at goldfish Mb1 synapses depends on GTP hydrolysis and is antagonized by a dynamin-interfering peptide (Jockusch et al., 2005), but additional evidence indicates a role for an ATP-dependent process that presumably is independent from dynamin (Heidelberger, 2001). Dynasore does not block endocytosis in mouse RB axon terminals, but it does switch the mode of vesicle recycling to favor bulk endocytosis (Logiudice et al., 2009).

Conclusion: dynamin deletion in rods as a model for ribbon synapse degeneration

The conditional deletion of dynamins 1 and 3 in rods induces a synapse degeneration of the rod with negative consequences for postsynaptic neurons. These features resemble some disease states, including retinal detachment (Wang et al., 2016; Townes-Anderson et al., 2021), age-related macular degeneration (Sullivan et al., 2007), and multiple sclerosis (Kesharwani et al., 2021) as well as normal aging (Samuel et al., 2011). Treatments for eye disease by cell transplantation can also disrupt photoreceptor synapses (Zarbin et al., 2019). The rod-specific deletion of dynamins 1/3 represents a model for studying synaptic degeneration that could be used to evaluate strategies for synapse repair and cell replacement therapies.

References

Antonny B, et al. (2016) Membrane fission by dynamin: what we know and what we need to know. EMBO J 35:2270–2284.

Arshavsky VY, Burns ME (2012) Photoreceptor signaling: supporting vision across a wide range of light intensities. J Biol Chem 287:1620–1626.

Berntson AK, Morgans CW (2003) Distribution of the presynaptic calcium sensors, synaptotagmin I/II and synaptotagmin III, in the goldfish and rodent retinas. J Vis 3:274–280.

Blanks JC, Johnson LV (1984) Specific binding of peanut lectin to a class of retinal photoreceptor cells. A species comparison. Invest Ophthalmol Vis Sci 25:546–557.

Brose N, Petrenko AG, Sudhof TC, Jahn R (1992) Synaptotagmin: a calcium sensor on the synaptic vesicle surface. Science 256:1021–1025.

Burger CA, Jiang D, Mackin RD, Samuel MA (2021) Development and maintenance of vision's first synapse. Dev Biol 476:218–239.

Cao Y, et al. (2009) Retina-specific GTPase accelerator RGS11/G beta 5S/R9AP is a constitutive heterotrimer selectively targeted to mGluR6 in ON-bipolar neurons. J Neurosci 29:9301–9313.

Cao Y, Posokhova E, Martemyanov KA (2011) TRPM1 forms complexes with nyctalopin in vivo and accumulates in postsynaptic compartment of ON-bipolar neurons in mGluR6-dependent manner. J Neurosci 31:11521–11526.

Chang B, et al. (2006) The nob2 mouse, a null mutation in Cacna1f: anatomical and functional abnormalities in the outer retina and their consequences on ganglion cell visual responses. Vis Neurosci 23:11–24.

Chapman ER, Hanson PI, An S, Jahn R (1995) Ca2 + regulates the interaction between synaptotagmin and syntaxin 1. J Biol Chem 270:23667–23671.

Dick O, tom Dieck S, Altrock WD, Ammermuller J, Weiler R, Garner CC, Gundelfinger ED, Brandstatter JH (2003) The presynaptic active zone protein bassoon is essential for photoreceptor ribbon synapse formation in the retina. Neuron 37:775–786.

Ding JD, Salinas RY, Arshavsky VY (2015) Discs of mammalian rod photoreceptors form through the membrane evagination mechanism. J Cell Biol 211:495–502.

Eisenfeld AJ, Bunt-Milam AH, Sarthy PV (1984) Muller cell expression of glial fibrillary acidic protein after genetic and experimental photoreceptor degeneration in the rat retina. Invest Ophthalmol Vis Sci 25:1321–1328.

Fan F, Funk L, Lou X (2016) Dynamin 1- and 3-mediated endocytosis is essential for the development of a large central synapse in vivo. J Neurosci 36:6097–6115.

Ferguson SM, et al. (2007) A selective activity-dependent requirement for dynamin 1 in synaptic vesicle endocytosis. Science 316:570–574.

Ferguson SM, et al. (2009) Coordinated actions of actin and BAR proteins upstream of dynamin at endocytic clathrin-coated pits. Dev Cell 17:811–822.

Ferguson SM, De Camilli P (2012) Dynamin, a membrane-remodelling GTPase. Nat Rev Mol Cell Biol 13:75–88.

Field GD, Rieke F (2002) Nonlinear signal transfer from mouse rods to bipolar cells and implications for visual sensitivity. Neuron 34:773–785.

Fox MA, Sanes JR (2007) Synaptotagmin I and II are present in distinct subsets of central synapses. J Comp Neurol 503:280–296.

Fuchs M, Brandstatter JH, Regus-Leidig H (2014) Evidence for a clathrin-independent mode of endocytosis at a continuously active sensory synapse. Front Cell Neurosci 8:60.

Furukawa T, Ueno A, Omori Y (2020) Molecular mechanisms underlying selective synapse formation of vertebrate retinal photoreceptor cells. Cell Mol Life Sci 77:1251–1266.

Grabner CP, Futagi D, Shi J, Bindokas V, Kitano K, Schwartz EA, DeVries SH (2023) Mechanisms of simultaneous linear and nonlinear computations at the mammalian cone photoreceptor synapse. Nat Commun 14:3486.

Grabner CP, Gandini MA, Rhak R, Le Y, Zamponi GW, Schmitz F (2015) RIM1/2-mediated facilitation of Cav1.4 channel opening is required for Ca2 -stimulated release in mouse rod photoreceptors. J Neurosci 35:13133–13147.

Grabner CP, Moser T (2021) The mammalian rod synaptic ribbon is essential for Cav channel facilitation and ultrafast synaptic vesicle fusion. Elife 10:e63844.

Grabner CP, Ratliff CP, Light AC, DeVries SH (2016) Mechanism of high-frequency signaling at a depressing ribbon synapse. Neuron 91:133–145.

Grassmeyer JJ, Cahill AL, Hays CL, Barta C, Quadros RM, Gurumurthy CB, Thoreson WB (2019) Ca(2+) sensor synaptotagmin-1 mediates exocytosis in mammalian photoreceptors. Elife 8:e45946.

Grossman GH, Ebke LA, Beight CD, Jang GF, Crabb JW, Hagstrom SA (2013) Protein partners of dynamin-1 in the retina. Vis Neurosci 30:129–139.

Haeseleer F, Imanishi Y, Maeda T, Possin DE, Maeda A, Lee A, Rieke F, Palczewski K (2004) Essential role of Ca2+-binding protein 4, a Cav1.4 channel regulator, in photoreceptor synaptic function. Nat Neurosci 7:1079–1087.

Hays CL, Sladek AL, Field GD, Thoreson WB (2021) Properties of multivesicular release from mouse rod photoreceptors support transmission of single-photon responses. Elife 10:e67446.

Hays CL, Sladek AL, Thoreson WB (2020) Resting and stimulated mouse rod photoreceptors show distinct patterns of vesicle release at ribbon synapses. J Gen Physiol 152:e202012716.

Heidelberger R (2001) ATP is required at an early step in compensatory endocytosis in synaptic terminals. J Neurosci 21:6467–6474.

Herrmann R, Lee B, Arshavsky VY (2011) RGS9 knockout causes a short delay in light responses of ON-bipolar cells. PLoS One 6:e27573.

Herrmann R, Lobanova ES, Hammond T, Kessler C, Burns ME, Frishman LJ, Arshavsky VY (2010) Phosducin regulates transmission at the photoreceptor-to-ON-bipolar cell synapse. J Neurosci 30:3239–3253.

Hovhannisyan A, Benkner B, Biesemeier A, Schraermeyer U, Kukley M, Munch TA (2015) Effects of the jimpy mutation on mouse retinal structure and function. J Comp Neurol 523:2788–2806.

Huh YJ, Choi JS, Jeon CJ (2015) Localization of rod bipolar cells in the mammalian retina using an antibody against the alpha1c L-type Ca(2+) channel. Acta Histochem Cytochem 48:47–52.
Imoto, et al. (2022) Dynamin is primed at endocytic sites for ultrafast endocytosis. Neuron 110:2815–2835.e13.
Ishibashi M, et al. (2022) Analysis of rod/cone gap junctions from the reconstruction of mouse photoreceptor terminals. Elife 11:e73039.
Ishikawa M, Sawada Y, Yoshitomi T (2015) Structure and function of the interphotoreceptor matrix surrounding retinal photoreceptor cells. Exp Eye Res 133:3–18.
Jeon CJ, Strettoi E, Masland RH (1998) The major cell populations of the mouse retina. J Neurosci 18:8936–8946.
Jockusch WJ, Praefcke GJ, McMahon HT, Lagnado L (2005) Clathrin-dependent and clathrin-independent retrieval of synaptic vesicles in retinal bipolar cells. Neuron 46:869–878.
Johnson J, Fremeau Jr RT, Duncan JL, Renteria RC, Yang H, Hua Z, Liu X, LaVail MM, Edwards RH, Copenhagen DR (2007) Vesicular glutamate transporter 1 is required for photoreceptor synaptic signaling but not for intrinsic visual functions. J Neurosci 27:7245–7255.
Kautzman AG, Keeley PW, Borhanian S, Ackley CR, Reese BE (2018) Genetic control of rod bipolar cell number in the mouse retina. Front Neurosci 12: 285.
Keeley PW, Patel SS, Reese BE (2022) Cell numbers, cell ratios, and developmental plasticity in the rod pathway of the mouse retina. J Anat 243:204–222.
Kerov V, et al. (2018) alpha2delta-4 is required for the molecular and structural organization of rod and cone photoreceptor synapses. J Neurosci 38: 6145–6160.
Kesharwani A, Schwarz K, Dembla E, Dembla M, Schmitz F (2021) Early changes in exo- and endocytosis in the EAE mouse model of multiple sclerosis correlate with decreased synaptic ribbon size and reduced ribbon-associated vesicle pools in rod photoreceptor synapses. Int J Mol Sci 22:10789.
Krizaj D, Copenhagen DR (1998) Compartmentalization of calcium extrusion mechanisms in the outer and inner segments of photoreceptors. Neuron 21:249–256.
Krizaj D, Demarco SJ, Johnson J, Strehler EE, Copenhagen DR (2002) Cell-specific expression of plasma membrane calcium ATPase isoforms in retinal neurons. J Comp Neurol 451:1–21.
Li S, Chen D, Sauve Y, McCandless J, Chen YJ, Chen CK (2005) Rhodopsin-iCre transgenic mouse line for Cre-mediated rod-specific gene targeting. Genesis 41:73–80.
Lobanova ES, Herrmann R, Finkelstein S, Reidel B, Skiba NP, Deng WT, Jo R, Weiss ER, Hauswirth WW, Arshavsky VY (2010) Mechanistic basis for the failure of cone transducin to translocate: why cones are never blinded by light. J Neurosci 30:6815–6824.
LoGiudice L, Matthews G (2007) Endocytosis at ribbon synapses. Traffic 8: 1123–1128.
Logiudice L, Sterling P, Matthews G (2009) Vesicle recycling at ribbon synapses in the finely branched axon terminals of mouse retinal bipolar neurons. Neuroscience 164:1546–1556.
Lou X, Paradise S, Ferguson SM, De Camilli P (2008) Selective saturation of slow endocytosis at a giant glutamatergic central synapse lacking dynamin 1. Proc Natl Acad Sci U S A 105:17555–17560.
Maddox JW, et al. (2020) A dual role for Ca(v)1.4 Ca(2+) channels in the molecular and structural organization of the rod photoreceptor synapse. Elife 9:e62184.
Mansergh F, Orton NC, Vessey JP, Lalonde MR, Stell WK, Tremblay F, Barnes S, Rancourt DE, Bech-Hansen NT (2005) Mutation of the calcium channel gene Cacna1f disrupts calcium signaling, synaptic transmission and cellular organization in mouse retina. Hum Mol Genet 14:3035–3046.
Masu M, Iwakabe H, Tagawa Y, Miyoshi T, Yamashita M, Fukuda Y, Sasaki H, Hiroi K, Nakamura Y, Shigemoto R, et al. (1995) Specific deficit of the ON response in visual transmission by targeted disruption of the mGluR6 gene. Cell 80:757–765.
Mattapallil MJ, Wawrousek EF, Chan CC, Zhao H, Roychoudhury J, Ferguson TA, Caspi RR (2012) The Rd8 mutation of the Crb1 gene is present in vendor lines of C57BL/6N mice and embryonic stem cells, and confounds ocular induced mutant phenotypes. Invest Ophthalmol Vis Sci 53:2921–2927.
Maxeiner S, Luo F, Tan A, Schmitz F, Sudhof TC (2016) How to make a synaptic ribbon: RIBEYE deletion abolishes ribbons in retinal synapses and disrupts neurotransmitter release. EMBO J 35:1098–1114.
Mercer AJ, Chen M, Thoreson WB (2011) Lateral mobility of presynaptic L-type calcium channels at photoreceptor ribbon synapses. J Neurosci 31:4397–4406.
Mercer AJ, Thoreson WB (2011) The dynamic architecture of photoreceptor ribbon synapses: cytoskeletal, extracellular matrix, and intramembrane proteins. Vis Neurosci 28:453–471.
Mesnard CS, Hays CL, Barta CL, Sladek AL, Grassmeyer JJ, Hinz KK, Quadros RM, Gurumurthy CB, Thoreson WB (2022) Synaptotagmins 1 and 7 in vesicle release from rods of mouse retina. Exp Eye Res 225: 109279.
Muller TM, et al. (2019) A multiple piccolino-RIBEYE interaction supports plate-shaped synaptic ribbons in retinal neurons. J Neurosci 39:2606–2619.
Neher E (2010) What is rate-limiting during sustained synaptic activity: vesicle supply or the availability of release sites. Front Synaptic Neurosci 2: 144.
Paisley CE, Kay JN (2021) Seeing stars: development and function of retinal astrocytes. Dev Biol 478:144–154.
Pangrsic T, Singer JH, Koschak A (2018) Voltage-gated calcium channels: key players in sensory coding in the retina and the inner ear. Physiol Rev 98: 2063–2096.
Park SJ, et al. (2020) Connectomic analysis reveals an interneuron with an integral role in the retinal circuit for night vision. Elife 9:e56077.
Pasteels B, Rogers J, Blachier F, Pochet R (1990) Calbindin and calretinin localization in retina from different species. Vis Neurosci 5:1–16.
Peichl L, Gonzalez-Soriano J (1993) Unexpected presence of neurofilaments in axon-bearing horizontal cells of the mammalian retina. J Neurosci 13:4091–4100.
Peichl L, Gonzalez-Soriano J (1994) Morphological types of horizontal cell in rodent retinae: a comparison of rat, mouse, gerbil, and guinea pig. Vis Neurosci 11:501–517.
Praefcke GJ, McMahon HT (2004) The dynamin superfamily: universal membrane tubulation and fission molecules? Nat Rev Mol Cell Biol 5: 133–147.
Qiao X, Pennesi M, Seong E, Gao H, Burmeister M, Wu SM (2003) Photoreceptor degeneration and rd1 mutation in the grizzled/mocha mouse strain. Vision Res 43:859–865.
Raimondi A, et al. (2011) Overlapping role of dynamin isoforms in synaptic vesicle endocytosis. Neuron 70:1100–1114.
Ramachandran R (2011) Vesicle scission: dynamin. Semin Cell Dev Biol 22: 10–17.
Reim K, Regus-Leidig H, Ammermuller J, El-Kordi A, Radyushkin K, Ehrenreich H, Brandstatter JH, Brose N (2009) Aberrant function and structure of retinal ribbon synapses in the absence of complexin 3 and complexin 4. J Cell Sci 122:1352–1361.
Ribic A, Liu X, Crair MC, Biederer T (2014) Structural organization and function of mouse photoreceptor ribbon synapses involve the immunoglobulin protein synaptic cell adhesion molecule 1. J Comp Neurol 522:900–920.
Robson JG, Frishman LJ (1998) Dissecting the dark-adapted electroretinogram. Doc Ophthalmol 95:187–215.
Robson JG, Frishman LJ (2014) The rod-driven a-wave of the dark-adapted mammalian electroretinogram. Prog Retin Eye Res 39:1–22.
Ronning KE, Allina GP, Miller EB, Zawadzki RJ, Pugh Jr EN, Herrmann R, Burns ME (2018) Loss of cone function without degeneration in a novel Gnat2 knock-out mouse. Exp Eye Res 171:111–118.
Sampath AP, Rieke F (2004) Selective transmission of single photon responses by saturation at the rod-to-rod bipolar synapse. Neuron 41: 431–443.
Samuel MA, Voinescu PE, Lilley BN, de Cabo R, Foretz M, Viollet B, Pawlyk B, Sandberg MA, Vavvas DG, Sanes JR (2014) LKB1 and AMPK regulate synaptic remodeling in old age. Nat Neurosci 17:1190–1197.
Samuel MA, Zhang Y, Meister M, Sanes JR (2011) Age-related alterations in neurons of the mouse retina. J Neurosci 31:16033–16044.
Sanuki R, Watanabe S, Sugita Y, Irie S, Kozuka T, Shimada M, Ueno S, Usukura J, Furukawa T (2015) Protein-4.1G-mediated membrane trafficking is essential for correct rod synaptic location in the retina and for normal visual function. Cell Rep 10:796–808.
Schmitz F (2009) The making of synaptic ribbons: how they are built and what they do. Neuroscientist 15:611–624.
Schmitz F, Konigstorfer A, Sudhof TC (2000) RIBEYE, a component of synaptic ribbons: a protein's journey through evolution provides insight into synaptic ribbon function. Neuron 28:857–872.

Sheng Z, Choi SY, Dharia A, Li J, Sterling P, Kramer RH (2007) Synaptic Ca^{2+} in darkness is lower in rods than cones, causing slower tonic release of vesicles. J Neurosci 27:5033–5042.

Sherry DM, Heidelberger R (2005) Distribution of proteins associated with synaptic vesicle endocytosis in the mouse and goldfish retina. J Comp Neurol 484:440–457.

Shi B, Jin YH, Wu LG (2022) Dynamin 1 controls vesicle size and endocytosis at hippocampal synapses. Cell Calcium 103:102564.

Specht D, Tom Dieck S, Ammermuller J, Regus-Leidig H, Gundelfinger ED, Brandstatter JH (2007) Structural and functional remodeling in the retina of a mouse with a photoreceptor synaptopathy: plasticity in the rod and degeneration in the cone system. Eur J Neurosci 26:2506–2515.

Spencer WJ, et al. (2019) PRCD is essential for high-fidelity photoreceptor disc formation. Proc Natl Acad Sci U S A 116:13087–13096.

Sterling P, Matthews G (2005) Structure and function of ribbon synapses. Trends Neurosci 28:20–29.

Sullivan RK, Woldemussie E, Pow DV (2007) Dendritic and synaptic plasticity of neurons in the human age-related macular degeneration retina. Invest Ophthalmol Vis Sci 48:2782–2791.

Thoreson WB (2021) Transmission at rod and cone ribbon synapses in the retina. Pflugers Arch 473:1469–1491.

Tien L, Rayborn ME, Hollyfield JG (1992) Characterization of the interphotoreceptor matrix surrounding rod photoreceptors in the human retina. Exp Eye Res 55:297–306.

Tom Dieck S, et al. (2012) Deletion of the presynaptic scaffold CAST reduces active zone size in rod photoreceptors and impairs visual processing. J Neurosci 32:12192–12203.

Tom Dieck S, Altrock WD, Kessels MM, Qualmann B, Regus H, Brauner D, Fejtova A, Bracko O, Gundelfinger ED, Brandstatter JH (2005) Molecular dissection of the photoreceptor ribbon synapse: physical interaction of bassoon and RIBEYE is essential for the assembly of the ribbon complex. J Cell Biol 168:825–836.

Townes-Anderson E, Halasz E, Wang W, Zarbin M (2021) Coming of age for the photoreceptor synapse. Invest Ophthalmol Vis Sci 62:24.

Van Hook MJ, Thoreson WB (2012) Rapid synaptic vesicle endocytosis in cone photoreceptors of salamander retina. J Neurosci 32:18112–18123.

van Rossum MC, Smith RG (1998) Noise removal at the rod synapse of mammalian retina. Vis Neurosci 15:809–821.

Vuong HE, de Sevilla Muller LP, Hardi CN, McMahon DG, Brecha NC (2015) Heterogeneous transgene expression in the retinas of the TH-RFP, TH-Cre, TH-BAC-Cre and DAT-Cre mouse lines. Neuroscience 307:319–337.

Wahl S, Katiyar R, Schmitz F (2013) A local, periactive zone endocytic machinery at photoreceptor synapses in close vicinity to synaptic ribbons. J Neurosci 33:10278–10300.

Waldner DM, Bech-Hansen NT, Stell WK (2018) Channeling vision: caV1.4-a critical link in retinal signal transmission. Biomed Res Int 2018:7272630.

Wang Y, et al. (2017) The auxiliary calcium channel subunit alpha2delta4 is required for axonal elaboration, synaptic transmission, and wiring of rod photoreceptors. Neuron 93:1359–1374 e6.

Wang J, Zarbin M, Sugino I, Whitehead I, Townes-Anderson E (2016) Rhoa signaling and synaptic damage occur within hours in a live pig model of CNS injury, retinal detachment. Invest Ophthalmol Vis Sci 57:3892–3906.

Wassle H, Puller C, Muller F, Haverkamp S (2009) Cone contacts, mosaics, and territories of bipolar cells in the mouse retina. J Neurosci 29:106–117.

Wen X, Van Hook MJ, Grassmeyer JJ, Wiesman AI, Rich GM, Cork KM, Thoreson WB (2018) Endocytosis sustains release at photoreceptor ribbon synapses by restoring fusion competence. J Gen Physiol 150:591–611.

Wu Y, O'Toole ET, Girard M, Ritter B, Messa M, Liu X, McPherson PS, Ferguson SM, De Camilli P (2014) A dynamin 1-, dynamin 3- and clathrin-independent pathway of synaptic vesicle recycling mediated by bulk endocytosis. Elife 3:e01621.

Xi Q, Pauer GJ, Ball SL, Rayborn M, Hollyfield JG, Peachey NS, Crabb JW, Hagstrom SA (2007) Interaction between the photoreceptor-specific tubby-like protein 1 and the neuronal-specific GTPase dynamin-1. Invest Ophthalmol Vis Sci 48:2837–2844.

Xu J, McNeil B, Wu W, Nees D, Bai L, Wu LG (2008) GTP-independent rapid and slow endocytosis at a central synapse. Nat Neurosci 11:45–53.

Yang J, Nan C, Ripps H, Shen W (2015) Destructive changes in the neuronal structure of the FVB/N mouse retina. PLoS One 10:e0129719.

Zarbin M, Sugino I, Townes-Anderson E (2019) Concise review: update on retinal pigment epithelium transplantation for age-related macular degeneration. Stem Cells Transl Med 8:466–477.